Parameterized internal wave mixing in three ocean general circulation models

Nils Brüggemann[1], Martin Losch[2], Patrick Scholz[2], Friederike Pollmann[4], Sergey Danilov[2], Oliver Gutjahr[1], Johann Jungclaus[1], Nikolay Koldunov[2], Peter Korn[1], Dirk Olbers[2,3], Carsten Eden[4]

[1]Max Planck Institute for Meteorology, Hamburg, Germany
[2]Alfred-Wegener-Institut, Helmholtz-Zentrum für Polar- und Meeresforschung, Bremerhaven, Germany
[3]Universität Bremen, Germany
[4]Institut für Meereskunde, Universität Hamburg, Germany

Key Points:

- the IDEMIX closure for a consistent representation of internal wave-induced mixing is evaluated in three state-of-the-art ocean models
- only in simulations with IDEMIX can the models reproduce the magnitude and spatial variability of the observed mixing work
- most changes with IDEMIX can be attributed to stronger mixing, but some effects are confounded by other processes and numerical mixing

Corresponding author: Nils Brüggemann, `nils.brueggemann@mpimet.mpg.de`

Abstract

The non-local model of mixing based on internal wave breaking, IDEMIX, is implemented as an enhancement of a turbulent kinetic energy closure model in three non-eddy resolving general circulation ocean models that differ in the discretization and choice of computational grids. In IDEMIX internal wave energy is generated by an energy flux resulting from near-inertial waves induced by wind forcing at the surface, and at the bottom, by an energy flux that parameterizes the transfer of energy between baroclinic and barotropic tides. In all model simulations with IDEMIX, the mixing work is increased compared to the reference solutions without IDEMIX, reaching values in better agreement with finestructure observations. Furthermore, the horizontal structure of the mixing work is more realistic as a consequence of the heterogeneous forcing functions. All models with IDEMIX simulate deeper thermocline depths related to stronger shallow overturning cells in the Indo-Pacific. In the North Atlantic, deeper mixed layers in simulations with IDEMIX are associated with an increased Atlantic overturning circulation and an increase of northward heat transports towards more realistic values. The response of the deep Indo-Pacific overturning circulation and the weak bottom cell of the Atlantic to the inclusion of IDEMIX is incoherent between the models, suggesting that additional unidentified processes and numerical mixing may confound the analysis. Applying different tidal forcing functions leads to simulation differences that are small compared to differences between the different models or between simulations with IDEMIX and without IDEMIX.

Plain Language Summary

Waves in the ocean interior play a fundamental role for ocean dynamics since they can carry energy over long distances and, once they break, lead to turbulent mixing. This turbulent mixing can cause dense water masses to rise from the deep ocean with a direct impact on large-scale currents. The wave dynamics occur on spatial scales that cannot be resolved in global ocean or climate models. To account for these processes, we apply the new parameterization IDEMIX that describes internal wave generation, propagation, and mixing. Using three different ocean models with and without IDEMIX ensures that we can identify model-specific effects of the parameterization and discriminate them from those independent of the model. We find that the simulated mixing patterns agree better with observations once IDEMIX is applied. Large-scale currents and the vertical temperature distribution are substantially affected by the internal wave parameterization. Whether this leads to an improved agreement with observed currents and water mass properties depends on the specific model and on numerical effects. In most cases, simulations with IDEMIX are not very sensitive to details of how the internal wave model is driven by tidal energy input.

1 Introduction

Turbulent mixing in the abyssal ocean associated with internal wave breaking provides the energy for diapycnal water mass transport. Besides other processes, such as wind driven upwelling and adiabatic advection, these diapycnal transports are key for the dense water masses to return to the surface and to close the meridional overturning circulation (see de Lavergne et al., 2022, for a recent review). Even though the energy flux from breaking waves to turbulence is so important, current ocean models typically do not parameterize this transfer in a consistent way. In this study, we aim to overcome this deficit and test the novel non-local energetically consistent parameterization IDEMIX (Internal Wave Dissipation, Energy and Mixing; Olbers & Eden, 2013). IDEMIX predicts internal wave propagation and dissipation based on the internal wave energy balance equation, and thus allows to parameterize wave-induced turbulent mixing based on the modeled climate state. We implement IDEMIX in three state-of-the-art ocean models to assess and compare their response to this new mixing scheme and to evaluate both model-specific effects and those that are independent of the individual model.

The internal waves, which are so crucial for the global circulation, are generated, for instance, by tidal or geostrophic flows over topography or by fluctuating winds (Olbers, 1983; Polzin & Lvov, 2011). As internal waves propagate through the ocean, they are subject to non-linear wave-wave interactions that transfer energy to shorter waves until the waves become unstable, break, and generate small-scale turbulence (see e.g., Müller et al., 1986; Musgrave et al., 2022). In addition, they interact with other features like mesoscale eddies, scatter at rough topography, or are affected by refraction or critical layer processes as the surrounding stratification changes (Olbers et al., 2019). Although some aspects of this complicated internal wave lifecycle can be resolved by state-of-the-art ocean models (e.g., Ansong et al., 2018), many are too small and fast and require additional non-hydrostatic dynamics so that they are not resolved in global ocean or climate models and will not be anytime soon. Instead, the effect of internal wave breaking and the associated diapycnal mixing has to be parameterized in these ocean models to account for the important driving mechanism of diapycnal mass transport.

In contrast to the complexity of the problem, interior mixing driven by internal wave-breaking is often parameterized in very simplistic ways. In particular, vertical mixing parameters are often chosen without taking into account energy constraints imposed by the sources of mixing. Instead, they are treated as tuning coefficients to optimize certain aspects of the respective model simulations. For some vertical mixing schemes, such as the PP (Pacanowski & Philander, 1981) or KPP (Large et al., 1994) schemes, it is common practice to parameterise internal wave mixing by a vertical diffusivity in the interior with a constant background coefficient of $\mathrm{O}(10^{-5}\,\mathrm{m}^2\,\mathrm{s}^{-1})$. Analogously, higher order mixing closures (e.g., Gaspar et al., 1990), impose a minimum (constant) turbulent energy with little physical motivation. The assumption behind these choices is that the internal wave field supplies a certain but unknown amount of energy to turbulent mixing. Neither approach, however, is physically consistent with the dynamics of internal waves, and they do not consistently represent the observed spatio-temporal variability of wave-induced turbulent mixing.

First attempts to link the parameterized mixing to the internal wave energetics were based on near-field tidal mixing parameterizations: Motivated by observations of enhanced mixing rates near rough topography, Simmons et al. (2004) assumed an ad-hoc length scale for the vertical shape and constructed a three-dimensional field of turbulent dissipation from a map of tidal energy conversion for the horizontal distribution to parameterize the spatio-temporal variability of wave-induced turbulent mixing. A refined version of this method linked the magnitude and scale height of the vertical dissipation profile to the internal wave shear represented by an idealized vertical wavenumber spectrum (Polzin, 2009). While these parameterizations successfully reproduce observed dissipation rates, they involve the specification of fixed parameters based on today's observations instead of the modeled, possibly changing, climate state, and moreover do not represent the horizontal propagation of wave energy, the scattering, refraction, or interaction processes that might occur during this propagation, or the dissipation and mixing associated with internal gravity waves other than high-mode internal tides.

In contrast, the parameterization framework IDEMIX (Olbers & Eden, 2013) explicitly accounts for internal wave physics in a consistent way: Based on the radiative transfer equation, it describes the rate of change of internal wave energy as a function of advection, refraction, generation, wave-wave interactions, and wave breaking (see Appendix B for details). All terms except for the generation are computed based on the resolved climate state. Wherever dependencies of internal wave characteristics on environmental conditions are unknown, these are determined from the Garrett-Munk reference spectrum (Garrett & Munk, 1972; Cairns & Williams, 1976), more specifically, from the shape of the spectrum in wavenumber-frequency domain (not the total energy content). External and constant forcing maps, representing mainly the effect of wind stress fluctuations at the ocean surface and flow-topography interactions at the ocean bottom describe the wave generation. The dissipated wave energy enters the turbulent kinetic energy (TKE) closure as an additional shear production term. This additional wave-induced TKE then determines the vertical mixing, that is, the vertical diffusivity κ in the ocean interior. This basic version of IDEMIX, which includes tidal, near-inertial, and lee wave mixing (the latter is not used in this study), was shown to successfully reproduce global patterns of ocean mixing inferred from Argo float profiles (Pollmann et al., 2017). Follow-up versions include the separation into low- and high-mode compartments (Eden & Olbers, 2014), wave-mean flow interactions (Olbers & Eden, 2017; Eden & Olbers, 2017), lee wave drag effects (Eden et al., 2021), and the application in the atmospheric context (Quinn et al., 2023).

Building on the IDEMIX compartment model (Eden & Olbers, 2014), de Lavergne et al. (2019, 2020) developed a tidal mixing scheme based on constant maps of internal wave energy dissipation, each representing a distinct dissipation process and associated with a distinct vertical distribution, derived from climatological stratification. The motivation to construct an energetically consistent mixing parameterization is hence common to all the parameterizations described in this section. However, IDEMIX is as of now the only operational framework to predict the mixing associated with different types of internal gravity waves based on the energy balance equation. Moreover, IDEMIX involves a two-way coupling where simulated internal wave energy and ocean stratification influence each other. This physically motivated representation of energy transfers between waves, turbulence, and mean flow allows energetically consistent, and hopefully more accurate ocean simulations also in a changing climate as long as the underlying assumption of constant external forcing holds or changes of the forcing could be somehow described.

Owing to limited observational data coverage, methodological constraints, or insufficient process understanding, the global quantification of internal wave generation is largely uncertain. One aim of this study is thus to estimate the uncertainty of key aspects of the ocean circulation caused by the uncertainty of the tidal forcing, the dominant internal wave generation mechanism (e.g. Musgrave et al., 2022). We focus on the basic version of IDEMIX (Olbers & Eden, 2013) with surface wind and bottom tidal forcing, and compare three simulations with different tidal forcing maps in IDEMIX. The reference simulation (without IDEMIX) uses a constant minimum background value for TKE to parameterize small-scale turbulence. The different forcing products are derived from (1) a scaling law for internal tide generation applied in barotropic ocean models using a bulk wave number for topography (referred to as forcing C, Jayne & St. Laurent, 2001), (2) a direct calculation from linear theory with a realistic bottom topography for eight tidal constituents (refferred to as forcinv B, Nycander, 2005; Falahat et al., 2014), and (3) estimates of internal tide generation from a high-resolution ocean model (Li & von Storch, 2020) for the M_2 tide complemented with seven most important other constituents from the linear theory calculation of (2) (reffered to as forcing A). The results are evaluated with respect to water mass biases, circulation changes, and mixing rates obtained from observations.

The effect of a given parameterization is often different for different models. To assess this effect, we use three different representative state-of-the-art ocean general circulation models: ICON-O (Korn et al., 2022), FESOM (Danilov et al., 2017), and MITgcm (Marshall et al., 1997; MITgcm Group, 2022). The models are very similar in their implementation of IDEMIX, share the same surface forcing in the momentum and tracer equations, and are similar albeit not equal in their vertical and horizontal resolution. The models also have substantial differences: most importantly, ICON-O and FESOM use (different) triangular grids in the horizontal, while the MITgcm uses a classical rectangular grid. ICON-O and the MITgcm use an Arakawa C-grid discretization, while FE-

Table 1. Most important features of the numerical models used in this study. Note that the effective horizontal resolution is difficult to compare on the different grids. Here we simply give the nominal grid spacing.

	ICON-O	FESOM	MITgcm
horizontal resolution	ca. 40 km	ca. 20–100 km	ca. 20–111 km
vertical levels	64	48	50
grid type	triangular	triangular	rectangular
grid staggering	C-grid	B-grid	C-grid

SOM uses an Arakawa B-grid. A complete description of similarities and differences of the three models is beyond the scope here; the reader is referred to the key references of the models given here and below. Despite these differences, the careful setup of comparable configurations and diagnostics allows us to investigate the model-independent effects of the IDEMIX closure with different forcing functions.

In the following Section 2, we describe the model setups and parameter choices in detail. In Section 3, we discuss the effect of IDEMIX on the mixing work for the different models and compare to available observations of mixing. In Section 4 the simulated water masses and in Section 5 the impact on the circulation are discussed. Finally, we investigate the impact of different tidal forcing functions in Section 6 before we discuss and conclude our results in Section 7.

2 Numerical model configurations and experiments

2.1 Model configurations

We employ three different numerical models with similar configurations: MITgcm, FESOM, and ICON-O. All model configurations were originally developed for other studies that did not include IDEMIX, and all model parameters are chosen according to their respective default values obtained from previous general model performance tuning. Here, we only standardize the vertical mixing parameterizations in all models without retuning the models. Some important model features are listed in Tab. 1. In all models, mesoscale eddies are not resolved but parameterized by a bolus velocity (Gent et al., 1995) and isopycnal diffusion (Redi, 1982). ICON-O uses a constant thickness mixing coefficient, FESOM employs a vertically varying coefficient following Ferreira et al. (2005), and the MITgcm simulation utilizes a horizontally varying coefficient based on horizontal and vertical buoyancy gradients (Visbeck et al., 1997). Furthermore, all three models differ in the numerical implementation of the parameterization as described in Korn (2018). The MITgcm and FESOM simulations use a vertical z^*-coordinate (Adcroft & Campin, 2004) that is rescaled to follow the local sea surface elevation, while ICON-O uses fixed z-levels. All models employ a non-linear free surface. More details about the specific model configurations can be found in Forget et al. (2015) for MITgcm, P. Scholz et al. (2022) for FESOM, and Korn et al. (2022) for ICON-O.

2.2 Atmospheric forcing

All simulations are forced by the same wind stress, surface heat and freshwater fluxes that are computed with the same bulk formulae (Large & Yeager, 2009) from the atmospheric fields of the 1958–2019 Japanese Re-Analysis dataset JRA55-do-v1.4.0 (Tsujino et al., 2018). Most of the presented results are from simulations that are integrated for 20 consecutive forcing cycles of 62 years, thus for 1240 years. However, some sensitivity simulations discussed in Section 6 are only integrated over five forcing cycles. In addition to applying freshwater fluxes, surface salinity is relaxed to an annual mean of the PHC-3.0 climatology (Steele et al., 2001) with a piston velocity of $10\,\mathrm{m}/60\,\mathrm{days} = 1.929\times 10^{-6}\,\mathrm{m\,s^{-1}}$. Initial conditions for temperature and salinity are derived from winter values of the PHC-3.0 climatology (Steele et al., 2001) in FESOM and MITgcm and from annual mean values for ICON (note that the slight differences of initial data are unlikely to have any effect for these long integration times). If not stated otherwise, we diagnose time averages over the last 40 years (1979–2019) of the last forcing cycle. Although the total integration time of 1240 years is too short for the simulations to fully equilibrate (see Fig. 8), it is long enough to study the major implications of vertical mixing on the water masses and circulation.

2.3 Experiments and tidal forcing

In all configurations, vertical mixing is parameterized by a second-order turbulent kinetic energy (TKE) closure (Gaspar et al., 1990; Blanke & Delecluse, 1993) (see Section Appendix A). The configurations with and without IDEMIX differ in their sources of TKE from internal wave dissipation. In each model, there are two different options for how the parameterized turbulent kinetic energy can be supplied in the interior. In the reference simulation, this source is determined by resetting the turbulent kinetic energy to a minimum background level of $1\times 10^{-6}\,\mathrm{m^2\,s^{-2}}$, implicitly assuming that an unspecified internal wave field always provides this level of energy for mixing in the ocean interior.

Once IDEMIX is used, the propagation and dissipation of the wave energy are predicted by a prognostic equation for internal wave energy. In other words, the TKE source that stems from internal wave dissipation is given by the parameterized dissipation term of the IDEMIX internal wave energy equation. All configurations using IDEMIX thus couple the equations for internal wave energy and turbulent kinetic energy via the wave dissipation (Olbers & Eden, 2013, see Appendix B). Therefore, the simulations with IDEMIX do not require an arbitrary minimum background level of turbulent kinetic energy, so it is set to zero (to avoid negative TKE due to numerics).

While IDEMIX hence avoids the arbitrariness and inconsistencies of pre-defining background energy levels (or specific aspects of the dissipation magnitude or profile as done in other wave-induced mixing schemes, e.g. Simmons et al., 2004), it requires the specification of internal wave energy forcing functions. At the surface, we use an update of the forcing product derived in Rimac et al. (2013) in all our IDEMIX simulations (see Figure 1 and Section Appendix B for details). This surface forcing product represents the process of wind-driven surface pumping (Olbers et al., 2020; von Storch & Lüschow, 2023) and the downward propagation of near-inertial internal waves generated at the base of the mixed layer by oscillations in the horizontal divergence of wind-driven currents in the surface mixed layer with frequencies at or above the local Coriolis frequency. At the bottom, we use in most simulations a combination of numerical and linear theory estimates of internal tide generation: the M_2-tide conversion derived from the STORMTIDE2 simulation (Li & von Storch, 2020) and the conversion into the seven other major constituents (S_2,N_2,K_2,K_1,O_1,P_1,Q_1) as computed by Falahat et al. (2014) following the methodology of Nycander (2005). These simulations are referred to as FESOM-A, ICON-A, and MITgcm-A. In Section 6, we also briefly discuss the influence of other available tidal forcing products, namely the forcing entirely derived from linear theory following Nycander (2005) (FESOM-B, ICON-B, and MITgcm-B), and the forcing as described in Jayne and St. Laurent (2001) (FESOM-C, ICON-C, MITgcm-C).

In the following, we only list the most important features of these three bottom forcing datasets and refer to a more detailed description in Appendix C. Forcing C (Figure 1d) is based on a scaling law for internal tide generation (and barotropic tide dissipation)

(Jayne & St. Laurent, 2001) that is motivated by linear theory (Bell, 1975b) and used in barotropic tidal models to represent the drag exerted by the baroclinic tides on the barotropic tides. The associated energy flux from this drag of the tidal flow, as diagnosed from a barotropic tidal model, is often used in a heuristic tidal mixing parameterization (Simmons et al., 2004), for example, in the CESM model (Hurrell et al., 2013). In this scaling law, the bottom topography spectrum is represented by one globally constant horizontal bulk wave number. This simplistic description and the uncertainty in choosing an appropriate bulk wavenumber implies that the internal tide generation may not be described very accurately in forcing C.

Alternatively, one can derive the bottom forcing directly from linear theory and realistic bottom topography at high resolution. For forcing B (Figure 1c), we use the estimates of Nycander (2005) as calculated by Falahat et al. (2014) for the eight major tidal constituents, computed for barotropic velocities from an inverse tidal model (Egbert & Erofeeva, 2002) and the observed topographic spectrum. However, both forcings B and C are subject to the limitations of linear theory, for example, when linear theory breaks down for topographic slopes steeper than that of the internal tide beam.

An alternative to such semi-analytical estimates is to estimate the tidal bottom forcing from internal tide generation in ocean general circulation models that are forced by the full tidal potential. We apply this method to derive the forcing dataset A (Figure 1b) from a concurrent simulation of circulation and tides by the Max Planck Institute Ocean Model simulation referred to as STORMTIDE2 (see Li and von Storch (2020) for details of the model setup and the computation of the internal tide generation). Restrictions of linear theory do not apply in such simulations, but the finite horizontal resolution (about 0.1°) allows only the first few vertical internal wave modes to be excited, and the parameterization of dissipation may introduce additional unknown model errors. Additionally, the conversion often becomes negative, which is not necessarily unphysical (Kelly & Nash, 2010), but it means that it cannot be used directly as a forcing term in IDEMIX (which is defined as positive). We remove negative values while preserving the original depth-dependent conversion rate following de Lavergne et al. (2019). The STORMTIDE2 simulation (Li & von Storch, 2020) includes the full luni-solar tidal forcing, but because other tidal constituents are less accurate, only the internal tide generation by the M_2 tide was calculated. Using the tidal energy generation only from the M_2 tide would miss roughly one third of the tidal energy. To compensate for this missing energy generation, we add to forcing A the energy generation from the seven most important other constituents according to Nycander (2005). Therefore, forcings A and B only differ with respect to the energy flux from the M_2 tide.

All tidal forcing datasets have in common that the energy flux is enhanced over major topographic obstacles such as sea mounts and ridges, for example, along the Mid-Atlantic Ridge (Fig. 1). The forcings A and B are in general smaller in magnitude than forcing C, especially in the Southern Ocean, and the global integral of forcing C (1.9 TW) is about two times larger than for B (1.0 TW) and A (0.9 TW). Note that forcing B only represents waters deeper than 400 m in order to discard the often supercritical topographic slopes in shallow waters, where the underlying linear theory breaks down. In contrast, forcing C includes the generation at all depths even though it is also based on a linear scaling law. Forcing C is much stronger on the continental shelves and slopes than the generation in the numerical model simulation or the semi-analytical estimate (forcing A and B), suggesting that it might not generally be applicable on the continental shelves but should only be used in the interior ocean. In practice, it has been used either in all depths (Jayne, 2009) or with a cut-off depth (Simmons et al., 2004, 1000 m). We follow Jayne (2009) in emphasizing the uncertainty of internal tide generation in realistic applications, where it is far from obvious how to correct for situations where nonlinear effects become important and the underlying linearity assumptions break down (see also e.g. Pollmann & Nycander, 2023). Considering that estimates from numerical model sim-

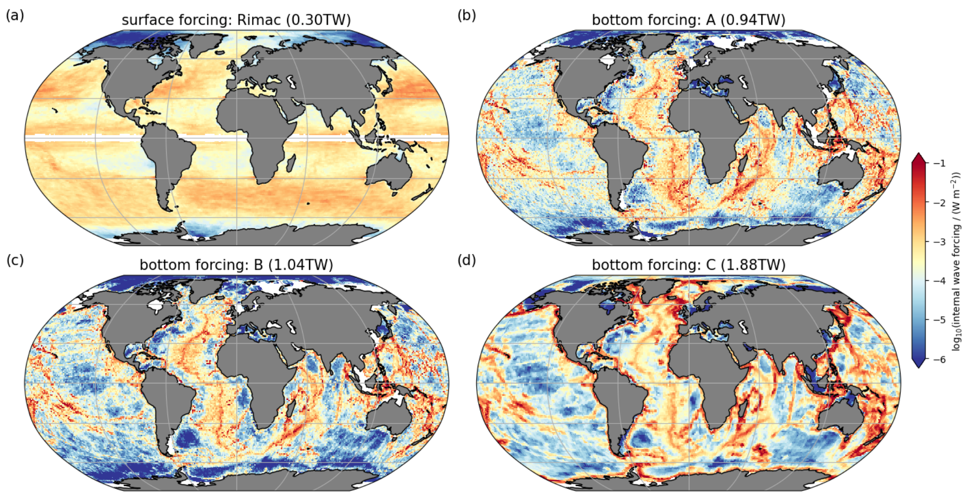

Figure 1. Energy flux into the internal wave field mapped to the ICON-O grid from (a) wind-driven near-inertial surface pumping from an update of Rimac et al. (2013) and the bottom (tidal) forcings A–C (b–d). See text for more details.

ulations suffer from other limitations (e.g. resolution or parameterization of unresolved processes) and that resolving these different uncertainties is subject to current research, we will use the three different estimates of internal tide generation in their unmodified form and consider their differences as plausible error bounds for the bottom forcing.

For the surface forcing, we use the same associated energy flux into the internal wave field for all IDEMIX simulations. This flux is derived from an updated product of the global estimate (Rimac et al., 2013) for the Climate Forecast System Reanalysis (CFSR) product (Saha et al., 2010). We account for the dissipation of the near-inertial motions within the mixed layer by multiplying the entire forcing product by a constant factor. This factor may vary geographically (Rimac et al., 2016; Olbers et al., 2020), but because our focus here is on the larger tidally induced forcing, we use a global constant of 20 % (Crawford & Large, 1996; Olbers & Eden, 2013). Note that the global integral of the internal wave forcing from the wind (0.3 TW, Figure 1a) is much smaller than the tidal forcing (Figures 1b–d).

3 Evaluation of mixing work and diffusivities

The primary source of small-scale turbulence in the interior ocean is internal wave breaking (e.g. Wunsch & Ferrari, 2004; Melet et al., 2022). In this way, the internal wave forcing controls the interior turbulent kinetic energy that is available for mixing of water mass properties. In our reference experiments, internal wave breaking is parameterized by resetting small turbulent kinetic energy values to an arbitrary constant minimum. In contrast, in simulations with IDEMIX, this energy source is parameterized based on physical principles. There are two major sinks of turbulent kinetic energy (TKE) in the interior ocean: (1) molecular dissipation (conversion of TKE into heat), and (2) the upward density flux associated with diapycnal mixing (transformation of TKE to mean potential energy). The upward buoyancy flux or mixing work is given by κN^2, with the diapycnal diffusivity κ and the buoyancy frequency N.

Since direct observations of small-scale turbulent mixing are sparse, we compare our model simulations with indirect estimates obtained from hydrographic profiles using the finestructure method (e.g. Gregg, 1989; Kunze et al., 2006; Polzin et al., 2014). The finestructure method links small-scale turbulence to finescale internal gravity wave variability based on a parameterization of wave energy dissipation through wave-wave interactions. It is important to note that this parameterization is also employed in IDEMIX (ϵ_{iw} in Eq. B1). The form for ϵ_{iw} was validated by numerical evaluation of the scattering integral for wave-wave interactions (Eden et al., 2019). The estimates derived from the finestructure method have a substantially larger uncertainty (by a factor of three or more according to e.g., Polzin et al., 2014; Pollmann et al., 2017) compared to turbulence estimates obtained from high-resolution shear or temperature observations (e.g. Fleury & Lueck, 1994; Waterhouse et al., 2014). However, when applied in regions where the underlying assumptions are met (i.e., away from boundaries or steep canyons), the finestructure parameterization was shown to successfully capture the mixing patterns of microstructure observations (e.g., Gregg, 1989; Wijesekera et al., 1993; Polzin et al., 1995; Whalen et al., 2015; Baumann et al., 2023).

For comparison between our model simulations and observations, we utilize: (a) an estimate of the vertical diffusivity and TKE dissipation rates from Argo float profiles (an updated version of Pollmann et al., 2017, Fig. 2g), (b) a database derived from the finestructure method applied to WOCE/CLIVAR hydrographic sections (Kunze, 2017, Fig. 3g), and (c) finestructure estimates from a hydrographic section at 48°N (Mertens et al., 2019, Fig. 4g). By definition, the finestructure method is only applied where $N^2 > 0$, so the mixing work derived from the observational data is always positive.

The mixing work κN^2 derived from observations varies by several orders of magnitude (Fig. 2–4). The global map derived from Argo float profiles (Fig. 2g) features relatively low values along the equator and over the abyssal plains. High values are found near mixing hot spots associated with rough bottom topography (e.g., the Hawaiian and Emperor Seamount Chains and the Izu-Bonin-Mariana arc system) and eddy activity (e.g., the Gulf Stream and Kuroshio regions). The general spatial pattern and magnitude are reproduced by all three models, but only in the simulations with IDEMIX (Fig. 2a–f). The horizontal structure in the IDEMIX simulations is a consequence of the spatially inhomogeneous internal wave forcing: especially the bottom forcing leads to increased internal wave energy levels at and, because of the horizontal spreading, near the generation hotspots, implying increased internal wave energy dissipation and thus mixing. In consequence, the horizontal structure of the mixing work in the simulations with IDEMIX resembles the forcing function (compare Fig. 2 to Fig. 1). In the reference simulations without IDEMIX, the mixing work is smaller and, as expected for a constant background turbulent kinetic energy, has little horizontal structure compared to the simulations with forcing A.

Inter-model differences can be found, for example, along the equator, where MITgcm-A produces relatively high mixing work compared to ICON-A and FESOM-A (compare Figure 2f with b, and d). This enhanced equatorial mixing is a consequence of a slightly different implementation of the regularization of the Coriolis parameter, which appears in the denominator of the expression for the internal wave dissipation and the group velocities (Equation B1 in Appendix B). Another difference is that in the ICON-A and MITgcm-A simulations, the mixing work increases abruptly over, for example, the Mid-Atlantic Ridge (see Figure 2b, d, and f). In the FESOM-A simulation, the mixing work appears to be stronger spread horizontally. We attribute this difference to smoother temperature and salinity fields as a consequence of different flux-limiting advection schemes employed within the different models. For all three models, however, the differences between the reference and IDEMIX simulations are substantially larger than the inter-model spread for either the reference or the IDEMIX simulations.

Along the WOCE section P15, which runs roughly along 170±5°W, mixing work from finestructure estimates (Kunze, 2017) decrease with depth from maximum values of $10^{-8}\,\mathrm{m^2s^{-2}}$ near the surface to minimum values of $10^{-11}\,\mathrm{m^2s^{-2}}$ and less at interme-

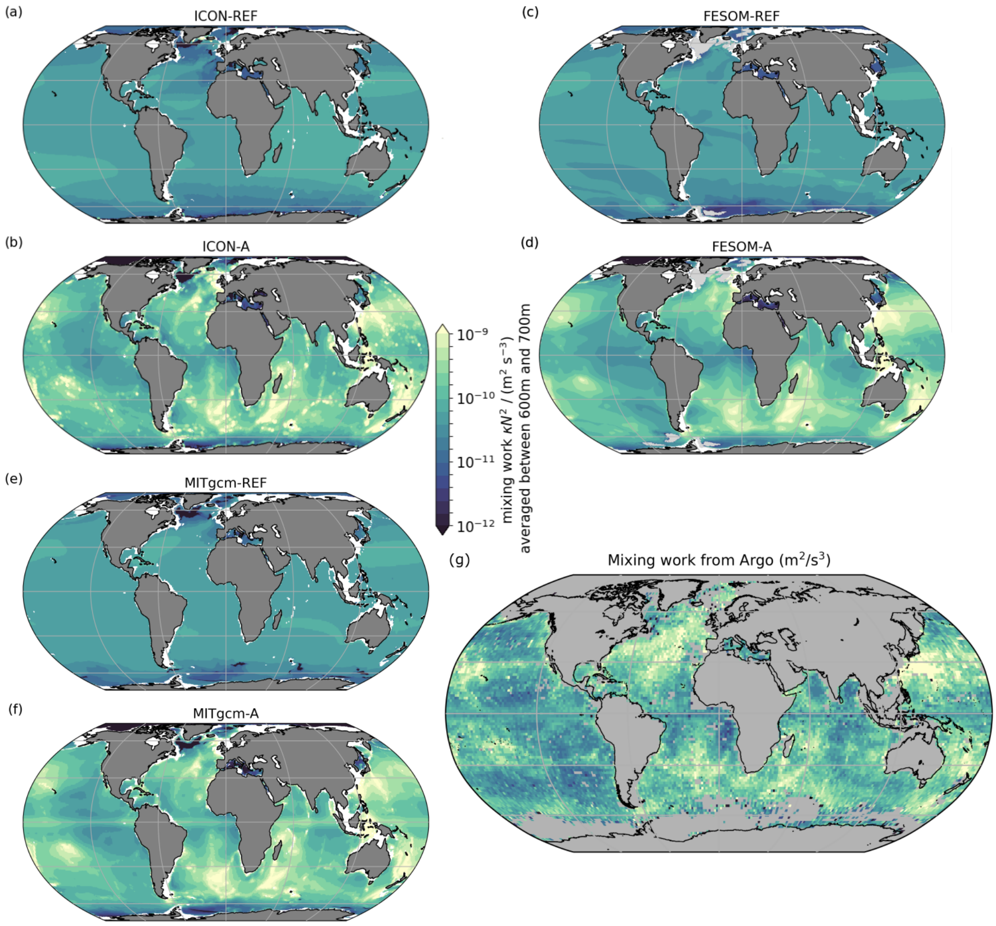

Figure 2. Mixing work κN^2 averaged between 600 m and 700 m. Subplots (a,b) show results from ICON-O, subplots (c,d) those from FESOM and subplots (e,f) those from the MITgcm. Note that κN^2 can be negative in regions of unstable stratification, mainly in the mixed layer. Since we do not focus on such situations, we masked these areas indicated by the light gray shading. (g) Mixing work κN^2 compiled from an update of the finestructure estimates of Pollmann et al. (2017).

diate depths and in some locations near the seafloor (Fig. 3g). Below 2000 m, these estimates are systematically lower than estimates from microstructure observations (de Lavergne et al., 2020). Exploring the reasons for these differences is beyond the scope this papers. Instead, we use Kunze (2017)'s data set as a reference in our evaluation of IDEMIX, but focus on the characteristics that we confirmed in our independent estimates from Argo float profiles (not shown): there are four maxima along the transect (roughly at 45°S, 30°S, 10°S and 20°N), which are associated with prominent topographic features (see also section 4). These are only reproduced by the models in the simulations with IDEMIX (Fig. 3b,d,f). In contrast to the always positive observational reference the model output can become negative (Fig. 3a–f). This is the case, for example, in the surface mixed layer, where it is associated with static instability (Figs. 3a–f). Negative values are also found at mid-depth in the ICON and MITgcm simulations as a result of preceding static instability in the course of deep convection during winter, or along the bottom slope in ICON and FESOM (Figs. 3b,f). In most places, however, the simulated κN^2 is positive, implying work done by mixing against the stable stratification, and roughly as strong as in the observational reference.

The comparison between observations and model output is similar for a section through the Atlantic at 48°N (Fig. 4). While the reference simulation has only little horizontal structure and, in particular, no increase of the mixing work over the Mid-Atlantic Ridge, the simulations using IDEMIX show a rich horizontal structure with high values over the Mid-Atlantic Ridge and in the western Atlantic, which is in much better agreement with observations than the mixing work simulated within the reference simulations. ICON and MITgcm show a minimum of the mixing work at roughly 1800 m depth when IDEMIX is applied, indicating a net convergence of buoyancy flux below this minimum. There is no such minimum in the FESOM-A simulation; instead the mixing work increases monotonically toward the surface in this simulation.

Note that there is no systematic increase in the mixing work with depth in the vertical sections along 170°W and the 48°N sections with and without IDEMIX. In our simulations with IDEMIX, we only occasionally observe bottom-intensified mixing work, for example, at the Mid-Atlantic Ridge at 48°N, where the mixing work increases close to the bottom and decays further up to 1500 m in ICON-A and MITgcm-A (note that FESOM-A shows no bottom-intensification at this location). Instead, the mixing work intensifies toward the surface, consistent with the finestructure observations. In steady state, upwardly increasing mixing work implies downward mixing balanced by (diapycnal) upwelling. This means that there is mostly upwelling along the 170°W and 48°N sections (except over the Mid-Atlantic Ridge in the 48°N section). In contrast, the scaling in Simmons et al. (2004) assumes that the mixing work decreases exponentially towards the surface implying downwelling.

For the simulations with IDEMIX, the total energy available for mixing is the global integral of internal wave forcing (Fig. 1), which amounts to 2.18, 1.34, and 1.24 TW for forcing A, B, and C, respectively (taking bottom and surface forcing together). For the reference simulations without IDEMIX, this available mixing energy is derived as the amount of energy required to keep the interior TKE at the depicted background value of $1\times10^{-6}\,\mathrm{m^2\,s^{-2}}$. Note that TKE dissipation and conversion of TKE to mean potential energy continuously reduce TKE, which means that keeping the TKE at a constant background value implies a source of TKE. Integrating this rate of change yields 0.37, 0.28, and 0.25 TW for ICON-REF, FESOM-REF, and MITgcm-REF, and consequently much lower mixing work than in the simulations with IDEMIX. In principle, we could increase the mixing work in the reference simulations by choosing a different background value for turbulent kinetic energy, but by doing so, the observed horizontal structure with its mixing hot spots will not be reproduced in the reference simulation. Therefore, we keep the commonly used background parameter (Blanke & Delecluse, 1993).

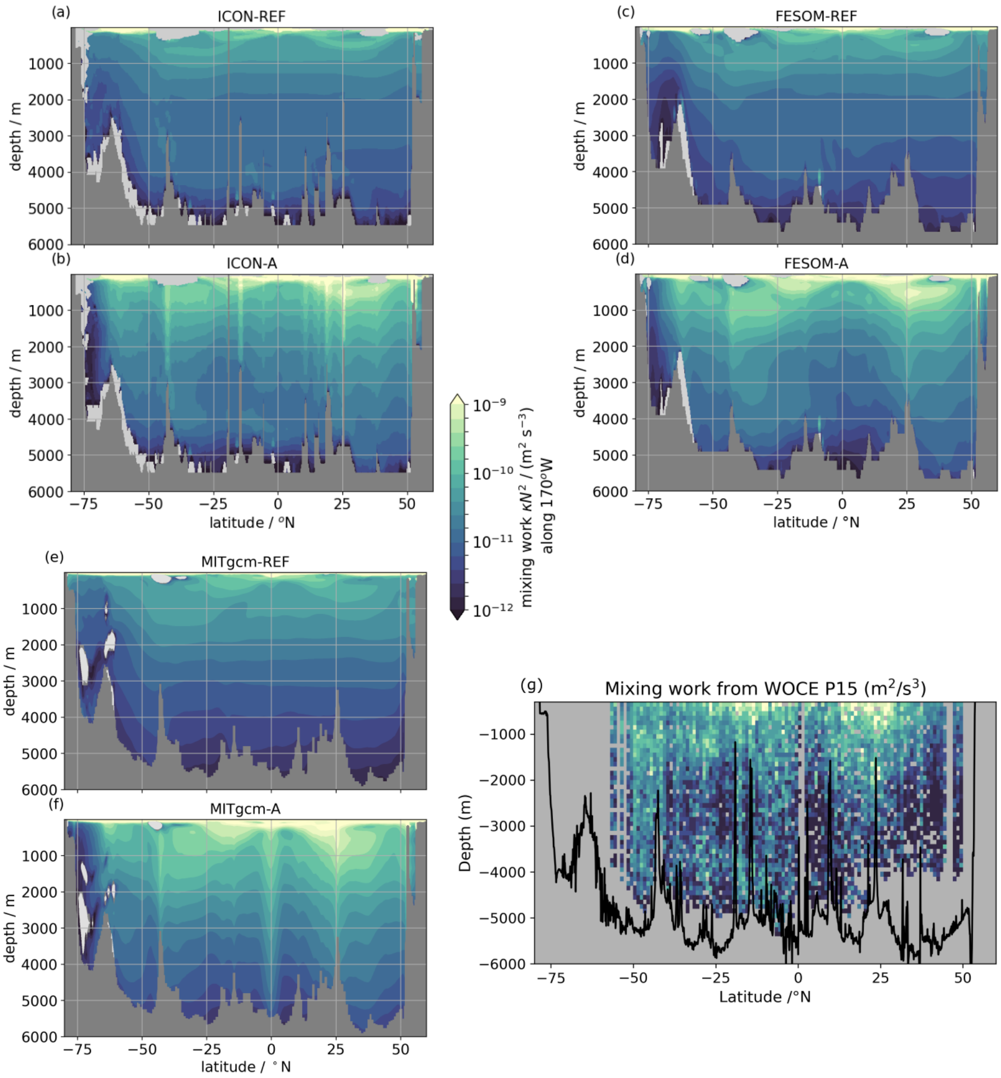

Figure 3. (a)-(f) Same as Fig. 2. but for a section in the Pacific along 170^{o}W. (g) Mixing work κN^2 compiled from the finestructure estimates of Kunze (2017) averaged between 164.9^{o}W and 165.1^{o}W north of the equator and between 169.9^{o}W and 170.1^{o}W at and south of it (WOCE section P15). The black line in g represents the bottom topography from Becker et al. (2009) (SRTM30+).

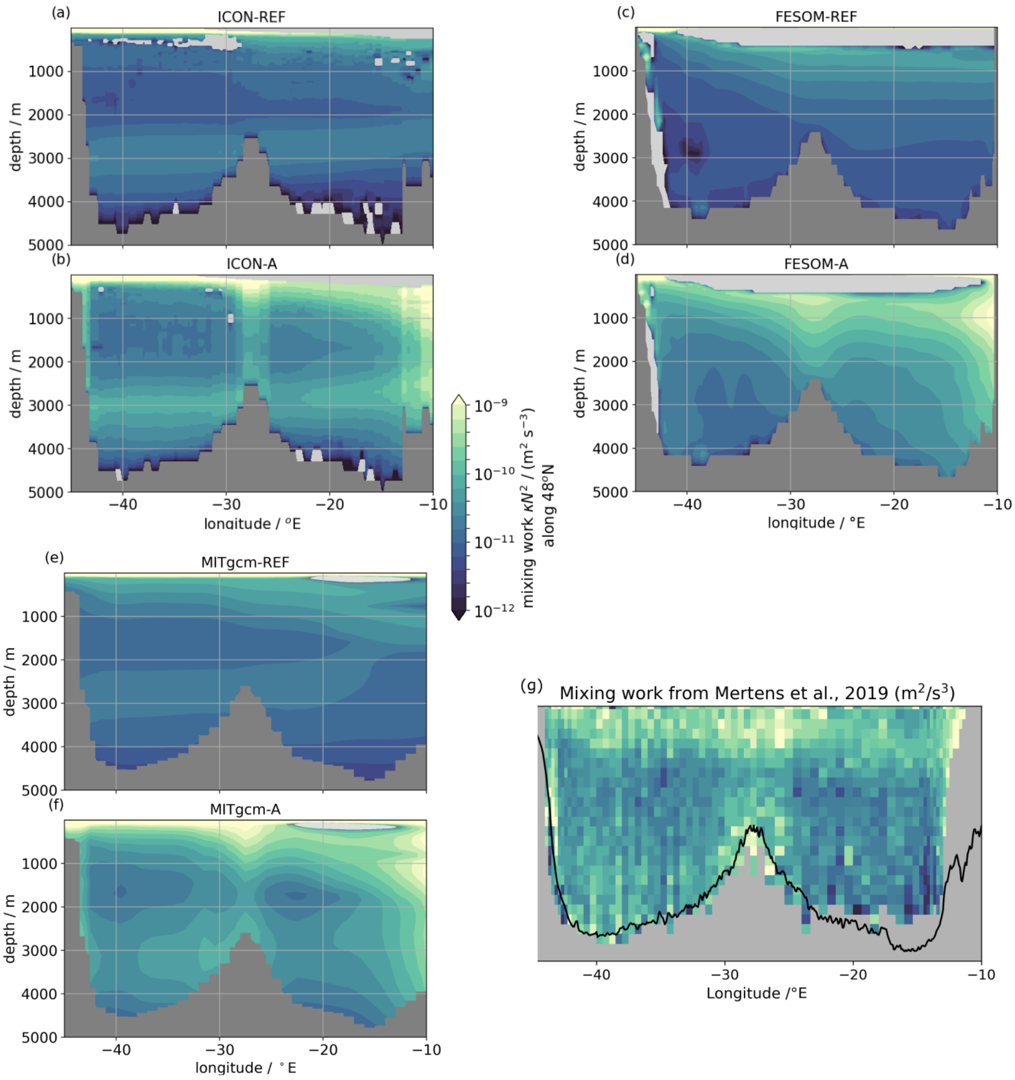

Figure 4. (a)-(f) Same as Fig. 2 but for a section across the Atlantic at 48°N. (g) finestructure estimates of mixing work from a hydrographic section at 48°N (Mertens et al., 2019).

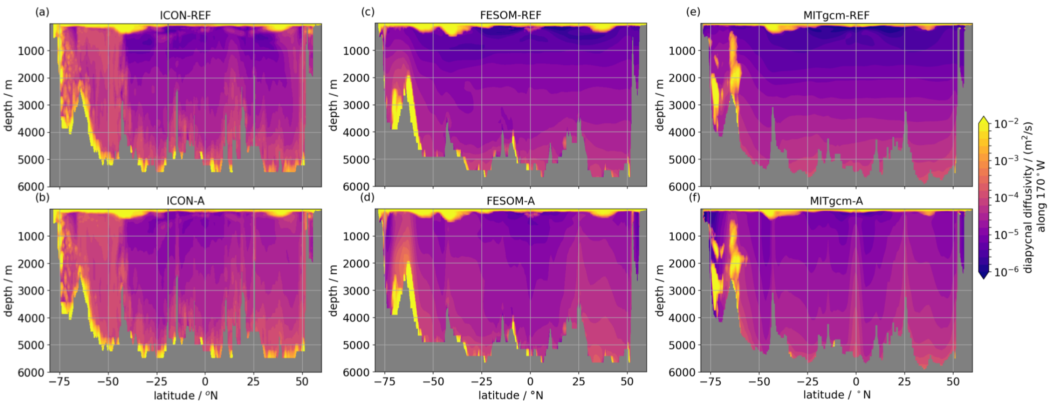

Figure 5. Diapycnal diffusivity κ along 170°W for ICON-O (a-b), FESOM (c-d) and MITgcm (e-f).

The vertical structure of the diffusivity (Fig. 5) differs from that of the mixing work (Fig. 5). In all simulations, diffusivities are high in the surface mixed layer as expected. Below the surface mixed layer, diffusivities decrease by orders of magnitude, but the diffusivities also increase again with depth with and without IDEMIX, meaning the increase is not related to the internal wave field but to the TKE mixing scheme and its dependence on the vertical stratification.

Similarly to the mixing work (Fig. 3), the horizontal variations of the diapycnal diffusivity κ are stronger when IDEMIX is applied (Fig. 5). One exception is ICON-REF, where an enhanced horizontal structure can also be found; this structure is accompanied by a similar structure in N^2 (not shown), such that the product κN^2 is smooth (Fig. 3a). In the MITgcm simulations, the diffusivities are also enhanced in the Southern Ocean between 1000 m and 3000 m, in accordance with the unstable conditions that occur in the simulations of this model (as discussed above). In general, all simulations with IDEMIX have higher diffusivities corresponding to the higher amount of energy available for mixing.

In summary, the rich spatial structure of the observed mixing work can only be reproduced in the simulations with IDEMIX, that is, a wave-induced mixing paramterization that accounts for the horizontal inhomogeneity of wave generation, propagation, and dissipation. Inter-model differences are associated with, among other things, differences in parameterization and numerical algorithms that are independent of the wave mixing closure. These differences are, however, substantially smaller than the differences between the simulations with and without IDEMIX.

4 Effects on water masses

The different levels of energy available for mixing have implications for water mass transformations in the model simulations. For all simulations, we observe that the vertical gradient of the mixing work is positive within the upper ocean in most areas. In the simulations with IDEMIX, this gradient is even increased, implying that surface and thermocline waters are more strongly mixed, leading to an enhanced downward buoyancy flux, and a deeper thermocline (Fig. 6, the thermocline depth is chosen to be the 12°C isotherm depth). All IDEMIX simulations produce comparable patterns of thermocline depth differences compared to the reference simulations. The differences are not uniform, and there are even locally shallower thermoclines with IDEMIX. The strongest increase in thermocline depth is found in the eastern tropical Pacific, the eastern sub-

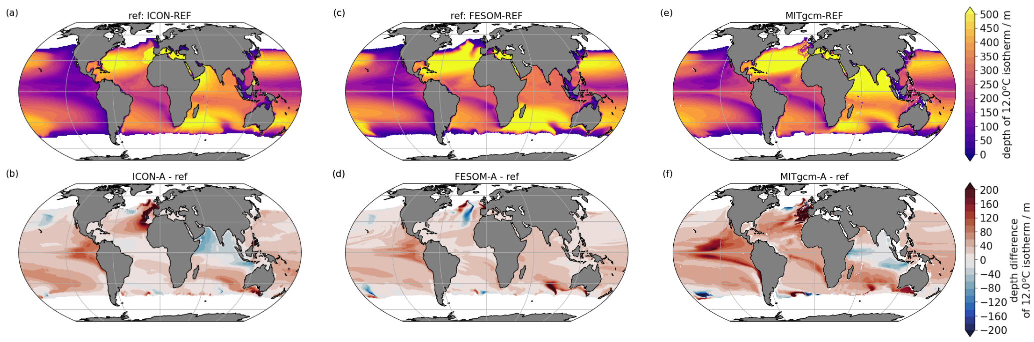

Figure 6. Depth of the 12^{o}C isotherm as a proxy of the thermocline depth. First column (a-b) shows results from ICON-O, second column (c-d) FESOM, and third column (e-f) MITgcm. The upper row shows results for the respective reference simulation, the lower row shows differences between the IDEMIX and the respective reference simulations.

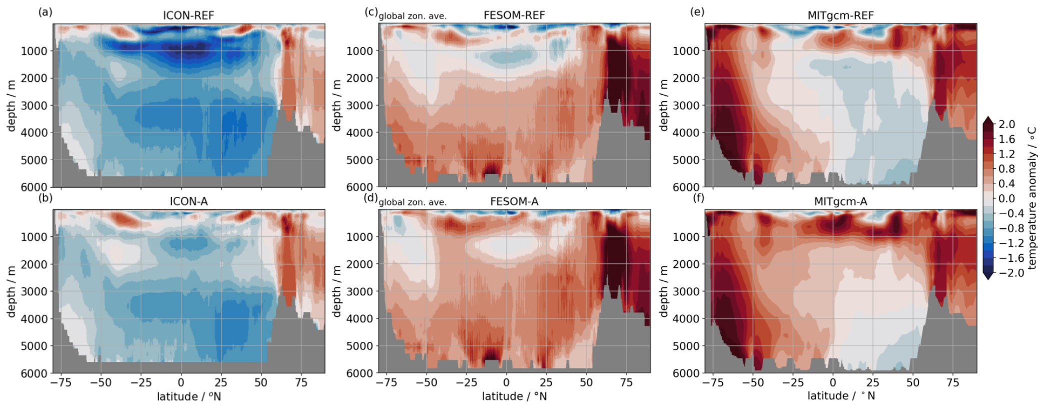

Figure 7. Zonal average of the temperature bias with respect to the PHC-3.0 climatology (Steele et al., 2001) for ICON-O (a-b), FESOM (c-d) and MITgcm (e-f).

tropical Atlantic, and the southern Indian Ocean, but these areas are not necessarily related to increased tidal forcing and wave dissipation, but rather resemble patterns of vertical stratification (not shown). The small regions of shallower thermocline depths are also consistent across the different model simulations, showing a coherent model response of the thermocline to changes in vertical mixing.

The enhanced vertical mixing due to IDEMIX also changes the temperature bias of the models. Relative to the PHC-3.0 climatology, the zonally averaged temperatures of ICON-REF are too low within the thermocline and too high close to the surface within 50°S and 50°N (Fig. 7a). The other models are too warm within the thermocline and too cold at the surface in the reference simulations (Fig. 7c and e). The stronger mixing in the IDEMIX simulations changes these biases because the stronger upper-ocean mixing decreases surface temperatures and increases temperatures within the thermocline. In ICON-O, IDEMIX reduces the cold bias of the reference simulation (Fig. 7b). The same mechanism increases the warm bias for the other two models with IDEMIX (FESOM-A and MITgcm-A), for which the thermocline waters are already too warm in the reference simulations (Fig. 7d and f).

There is a prominent warm temperature bias in the North Atlantic at 50°N that does not change with IDEMIX (supplementary Fig. 1). This bias is related to the miss-

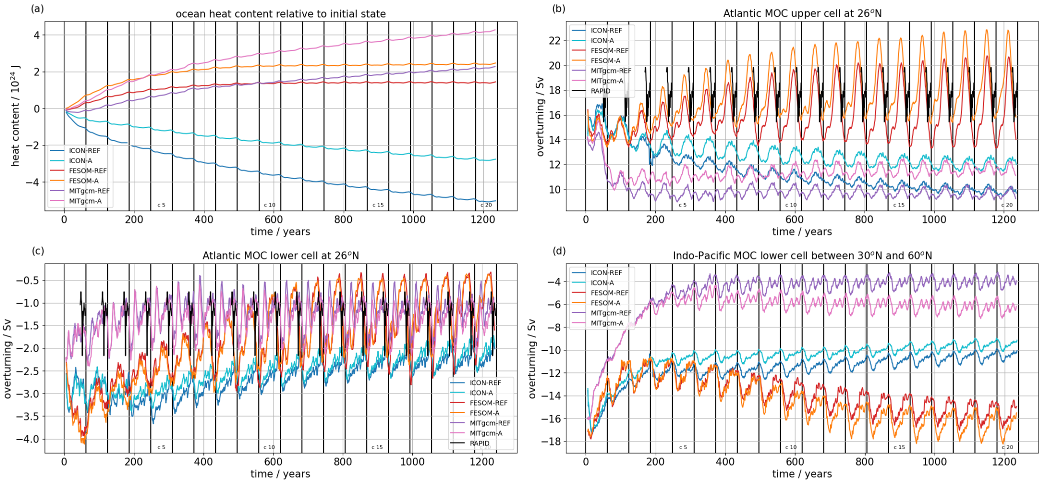

Figure 8. Timeseries of (a) ocean heat content relative to initial conditions, (b) maximum of Atlantic MOC at 26°N within the depth range of 500 m to 1500 m, (c) minimum of Atlantic MOC at 26°N within the depth range of 1500 m to 6000 m, and (d) minimum of Indo-Pacific MOC in between 30°S and the equator and within the depth range of 1500 m to 6000 m. Black lines in (b) and (c) indicate observational data derived from the RAPID array measurements (Smeed et al., 2018). Black vertical lines mark the end of a forcing cycle. All model data shown in this figure is averaged by an 11 year running mean.

ing northwest corner of the North Atlantic Current. It is a common feature of many non-eddy-resolving models that cannot resolve the interaction of mesoscale eddies with topography, which is most likely responsible for northward recirculation of the North Atlantic Current (Zhai et al., 2004). Insufficient representation of overflow dynamics in coarse models may also contribute to the missing northwest corner. Since the warm bias at 50°N in the North Atlantic is unrelated to vertical mixing and our models do not resolve eddy-topography interaction nor represent the overflows correctly, not much change of this bias is to be expected once IDEMIX is used.

In general, 1240 years (20 forcing cycles) are not sufficient for the ocean circulation to reach equilibrium. The residual trend for the temperature development can be inferred from Fig. 8a. Note that both ICON simulations continue to cool, while the MITgcm simulations continue to warm, and only for the FESOM simulations does the ocean heat content appear to be stable. These general biases in the ocean heat content can be tuned by adjusting the c_k parameter of the TKE scheme. For example, the temperature bias was successfully reduced in ICON-O with a larger $c_k = 0.3$ instead of 0.1 (Korn et al., 2022; Hohenegger et al., 2023). Tuning this parameter (and others) will most likely lead to different parameter sets for each model. For this reason, and to stay as close as possible to the standard literature values, no tuning was attempted in this study.

The mixed layer depths in the subpolar North Atlantic (supplementary Fig. 2) are increased in all models and experiments with IDEMIX compared to the respective reference simulations, particularly in deep water formation sites such as the Nordic Seas, Irminger Sea, and Labrador Sea. The deeper mixed layers are most likely caused by the stronger internal mixing with IDEMIX, which reduces the stratification below the mixed layer base. We refer to this process as preconditioning by internal mixing.

In MITgcm-REF and ICON-REF, the mixed layer depths in the subpolar North Atlantic are in good agreement with observations (supplementary Fig. 4, Locarnini et

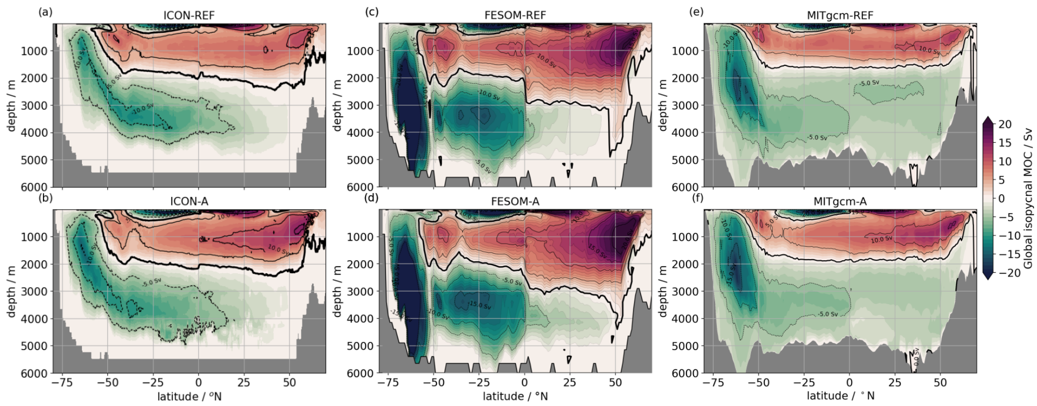

Figure 9. Global meridional overturning stream function ψ in Sv. ψ was calculated in density space and remapped to depth levels for ICON (a-b), FESOM (c-d) and MITgcm (e-f).

al., 2018; Zweng et al., 2019) while FESOM-REF tends to produce too deep convection depths. In FESOM, IDEMIX increases the bias by deepening and widening the already too deep and wide convection zone. The deeper mixed layers are associated with an increase in the Atlantic meridional overturning circulation, as will be discussed in the next section.

5 Effects on the circulation

The global meridional overturning stream function ψ is calculated in potential density space. Diapycnal transports are computed from the divergence of time averages of horizontal transports in 88 σ_2 layers with a reference pressure of 2000 dbar and then integrated in the meridional direction to obtain a stream function in density space. This stream function is remapped to depth coordinates $z(\bar{\sigma}_2)$, where $\bar{\sigma}_2$ denotes the zonal average of σ_2. The stream function based on averages on density levels illustrates the actual water mass transports and avoids artifacts such as the Deacon Cell in the Southern Ocean typically seen in Eulerian averages along constant z-levels (McDougall & McIntosh, 2001).

All simulations show the familiar two-cell structure of the global overturning (Fig. 9). The upper cell in the northern hemisphere is generally stronger and deeper for FESOM than for MITgcm and ICON. The lower cell in the southern hemisphere is strongest in FESOM and weakest in MITgcm.

When the global stream function is decomposed into Atlantic and Indo-Pacific basins the differences between the models are also greater than between experiments of the same model with and without IDEMIX (Fig. 10 and 12). In all models, the Atlantic upper cell increases by up to 5 Sv but the vertical shape of this increase is different between models (Fig. 10). The increased overturning is related to deeper mixed layers, indicative of increased deep water formation, in the subpolar North Atlantic in each of the experiments with IDEMIX (Supplement Fig. 2). The relationship between deep convection and the strength of the overturning is often observed in ocean models (e.g., Eden & Jung, 2001), but the connection between deep water formation and overturning is still not fully understood (e.g., Brüggemann & Katsman, 2019; Lozier et al., 2019; Georgiou et al., 2021).

Compared to observations (e.g., Lumpkin & Speer, 2007), the upper cell of the Atlantic overturning is too weak in all reference simulations, particularly in the subtropics and in MITgcm-REF. Furthermore, the upper cell of the stream function is too shal-

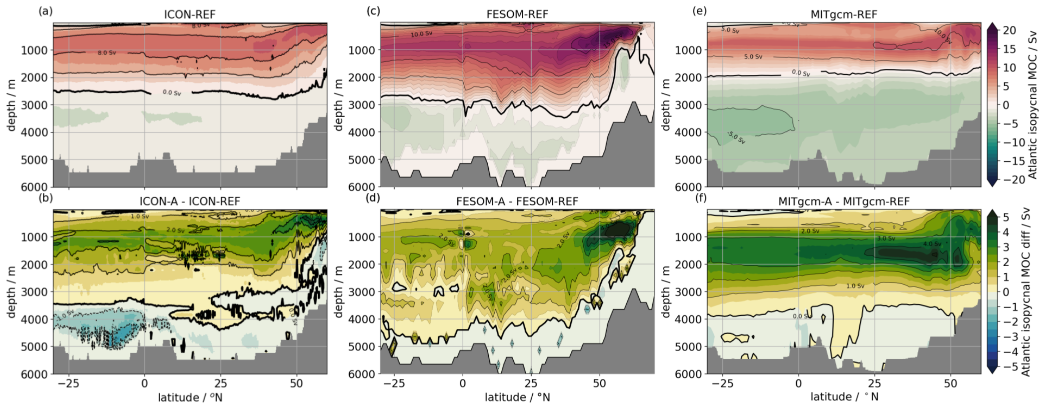

Figure 10. Same as Figure 9 but for the Atlantic basin only. Reference simulations of (a) ICON-O, (c) FESOM (e) and MITgcm, and (b,d,f) difference of ψ between the simulations with forcing A and the reference simulation.

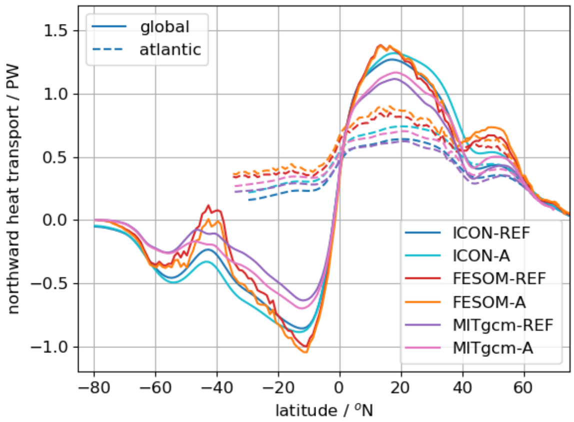

Figure 11. Northward heat transport in PW for the global ocean (solid lines) and the Atlantic ocean only (dashed lines).

low (see Korn et al., 2022; Jungclaus et al., 2022). The common response to the inclusion of IDEMIX is that all models converge to the observations, thereby increasing the northward heat transports in the Atlantic Ocean (compare Fig. 11). Still, no model succeeds in reproducing the observed heat transport (more than 1 PW), although the simulations using IDEMIX show a somewhat stronger and thus improved Atlantic heat transport. Changes in the Atlantic lower cell are weak and incoherent between the models (Fig. 10), a feature also seen in the bottom cell of the Indo-Pacific, discussed below.

In the Indo-Pacific basins, the strength of the southern upper shallow overturning cell within the thermocline increases in all models with IDEMIX compared to the reference simulations (Fig. 12). North of the equator, a similar increase of the shallow cell is also seen in ICON-O and MITgcm, but only to a weaker extent in FESOM. The common model response of stronger upper cells to larger mixing work is surprising, because the shallow cells within the thermocline are thought to be driven by the wind and not the vertical mixing. The strengthening, however, can be explained by a deeper thermocline in these simulations (Fig. 6) that could lead to larger areas of the subducting den-

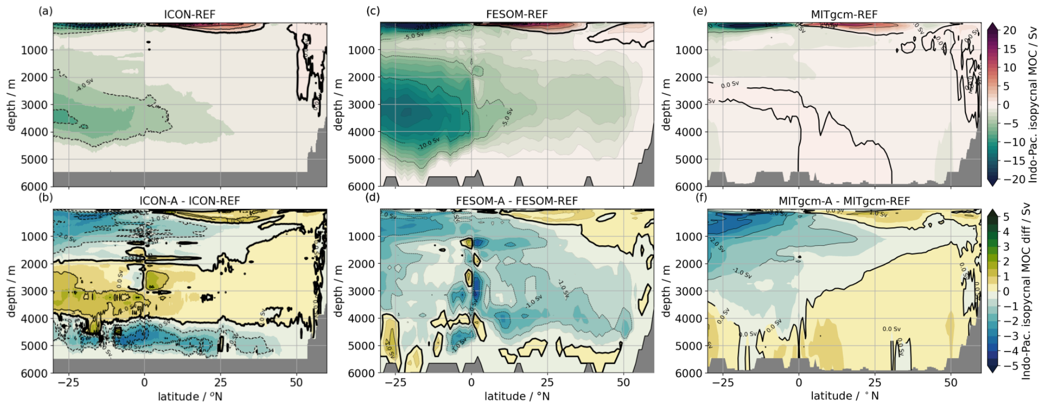

Figure 12. Same as Fig. 10, but for the Indo-Pacific basin.

sity layers exposed to the atmosphere, and thus stronger ventilation and stronger overturning.

Substantial changes can be found in the Indo-Pacific bottom cell (Fig. 12), but there is no coherent response among the models, similar to the Atlantic bottom cell. Lumpkin and Speer (2007) found a global net overturning of dense water masses of 20.9±6.7 Sv across 32°S and other observational estimates yield similar transports into the Pacific (Ganachaud, 2003; Talley et al., 2003; Schlitzer, 2007). This overturning rate is not reproduced by any model (even for the unrealistic case FESOM-C, see Fig. 14). The reason for this model bias, and in particular the reason for the incoherent model response in the bottom cell in the Indo-Pacific and Atlantic Ocean, remains unclear. We discuss this aspect in Section 7.

The time series of the overturning during the entire 1240 years (20 forcing cycles) at different locations (Fig. 8b-d) show that the circulation is still not at an equilibrium, not even for the FESOM simulations where the total heat content was nearly in equilibrium (Fig. 8a). Nevertheless, a clear reduction of the trends can be identified after roughly four forcing cycles, and we do not expect any further qualitative changes after the 1240 years of simulation.

Although all simulations begin with similar overturning strengths, they start to diverge quickly in the first forcing cycle. The upper cells of the overturning in the ICON and MITgcm simulations decrease substantially below observations at the RAPID array (e.g., Smeed et al., 2018), while there is a slight increase for FESOM (Fig. 8b). For MITgcm and ICON, the simulations with IDEMIX have a 2 Sv stronger overturning and are therefore closer to observations. The lower Atlantic overturning cell (Fig. 8c) starts too strong with ICON and MITgcm but both models reduce the overturning strength towards observational estimates from the RAPID array. In FESOM, the lower Atlantic overturning cell remains relatively stable and close to the observed values. For all three models, including IDEMIX makes only a small difference in the strength of the lower Atlantic overturning cell. For the Indo-Pacific, the difference between reference simulation and the forcing A simulation is roughly 1 Sv for ICON and MITgcm and 2 Sv for FESOM. While the Indo-Pacific overturning increases for FESOM and MITgcm, it decreases for ICON.

6 Effects of different tidal forcing products

Since the bottom forcing for IDEMIX is the largest source of internal wave energy, we analyze the effects of different forcing products within this section. So far, we concentrated our discussion on forcing A derived from the STORMTIDE2 simulation (Li & von Storch, 2020) for the M_2 constituent and from linear theory after Nycander (2005) for the seven most important other constituents. Now, we will also consider forcing B derived solely from linear theory after Nycander (2005) and forcing C based on the parameterization of drag by internal tide generation (Jayne & St. Laurent, 2001). To save computer resources, all simulations using forcing B and C were only run for five forcing cycles (310 years), and we thus compare, in this section, averages from year 270 to 310 for all simulations (REF and A-C).

In all forcing products, the internal wave bottom forcing is large over topographic obstacles such as the Mid-Atlantic Ridge and small where the bathymetry is flat, such as in the Argentinian Basin (Fig. 1). Forcing B is similar to our standard forcing A but contains slightly higher energy fluxes and has larger maximum energy fluxes over ridges, and smaller minimum fluxes in the deep basins. Also, spatial gradients are generally smaller. Forcing C (Jayne & St. Laurent, 2001) has substantially higher fluxes in coastal regions, especially in the Southern Ocean, and the total energy flux is about 1.8 times larger than in forcing A.

Naturally, the different forcing products will lead to different amounts of mixing work. As already discussed in Section 3, the mixing work κN^2 along 170°W is very low in all reference solutions without IDEMIX, and its variation is almost negligible (Fig. 13a). With IDEMIX, all models generate more mixing work and reproduce the observed minima at higher latitudes (see also Gutjahr et al., 2021) and near the equator as well as the maxima at around 45°S and 20°N (Fig. 13b–d). The experiments with forcing C tend to have slightly larger κN^2 than the other forcings, consistent with the larger energy in forcing C, but all simulations agree roughly in the location and magnitude of the mixing hot spots. For each model, the difference between the sensitivity simulations with different tidal forcings is smaller than the difference to the reference experiment. All simulations with IDEMIX, independent of the forcing, overestimate the mixing work in the North Pacific, but the simulations with forcing C also grossly overestimate the mixing work in the Southern Ocean, particularly FESOM-C. We conclude that forcing A and B appear to produce more realistic magnitudes of the mixing work compared to forcing C.

The additional energy input in forcing C also has important implications for the circulation for some models (Fig. 9). The largest difference in overturning is a substantially stronger bottom cell in FESOM-C. The stronger forcing C leads to more mixing work, which then triggers exaggerated deep water formation in the Southern Ocean, as can be inferred from the increased bias towards deeper mixed layers in this simulation (supplementary Fig. 3). In MITgcm-C, we also find a slightly enhanced strength of the deep cell, while in ICON-C there is hardly any change, if not a slight weakening of the bottom cell with forcing C. Except for the deep cell in the Southern Ocean, the differences in the overturning stream functions with different forcings remain relatively small compared to the differences between the models.

We find that the enhanced mixing with IDEMIX also leads to deeper winter mixed layers in the North Atlantic (supplementary Fig. 2) and deeper summer mixed layers in the Southern Ocean (supplementary Fig. 3), particularly for forcing C. The increased interior mixing leads to stronger preconditioning, which in turn drives more deep convection. In the case of FESOM C, the mixed layer depths become unreasonably deep in the Southern Ocean, indicating increased bottom water formation, which is reflected by the stronger overturning (see Fig. 9h). The mixed layer depths in MITgcm-C and ICON-C are also exaggerated in comparison to observations (supplementary Fig. 4), but with forcing A and B, the region of deep mixing in the Southern Ocean increases and tends

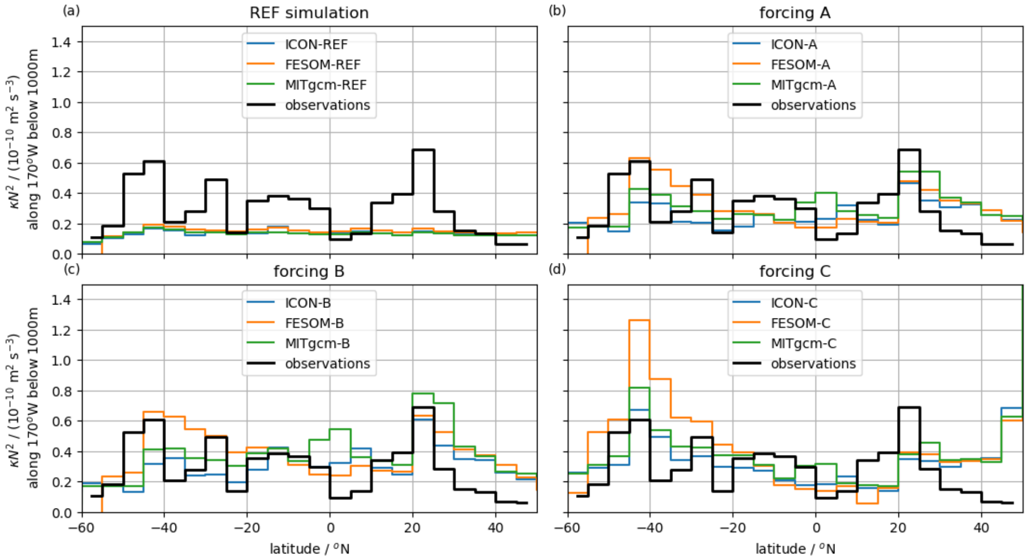

Figure 13. Mixing work along 170^{o}W in the South Pacific and along 165^{o}W in the North Pacific. Results are averaged below 1000 m and over the last 40 years of the fifth forcing cycle. The reference simulation is shown in (a), and the IDEMIX simulations with forcing data A, B, and C are shown in (b), (c), (d), respectively. The black line represents the corresponding results for the observed mixing work shown in Fig. 3g. All results are binned in 5° latitude intervals.

to be in better agreement with the observations compared to the reference simulations without IDEMIX.

7 Summary and conclusions

A vertical mixing scheme based on internal wave physics (IDEMIX) is implemented and evaluated in three different ocean models: ICON-O, FESOM, and MITgcm. The implemented version of IDEMIX (Olbers & Eden, 2013) predicts the bulk wave energy propagation and dissipation driven by the wave forcing functions at the top and the bottom of the ocean. The internal wave energy dissipation provides forcing to a turbulent kinetic energy (TKE) mixing closure (Gaspar et al., 1990). The surface forcing of internal waves is much smaller than the bottom sources, and we concentrate on three different products for the larger bottom forcing, representing tidal flow over topography: forcing A is based on the M_2-tide generation derived from a global high-resolution ocean model simulation (STORMTIDE2) with tidal forcing (Li & von Storch, 2020) and the seven most important other tidal constituents from linear theory (Nycander, 2005; Falahat et al., 2014); forcing B is calculated from linear theory alone (Nycander, 2005; Falahat et al., 2014); and forcing C is based on the drag parameterization by internal tide generation of a barotropic tidal model (Jayne & St. Laurent, 2001).

While forcing A is subject to biases from limited horizontal resolution, dissipation, and other unknown biases of the high-resolution STORMTIDE2 simulation, forcing B suffers from the limitations of linear theory associated with the underlying weak topography assumption (i.e., gentle topographic slopes and small tidal excursion). Finally, forcing C is subject to the biases associated with its simplistic nature (i.e., a globally constant representative wave number for the topography) as well as of the barotropic tide model for which the drag parameterization accounts. Accordingly, the forcing functions differ by almost a factor of two in the global integrated flux into the wave field, where

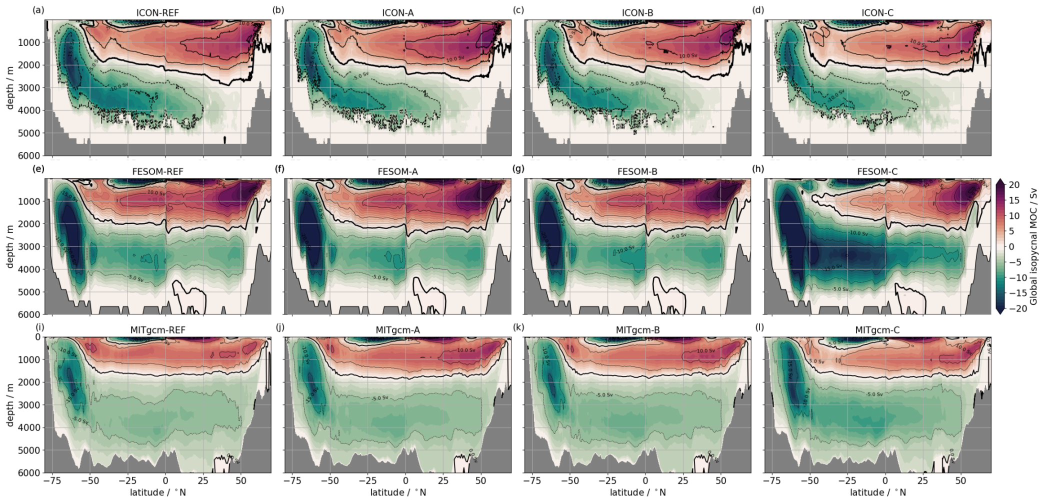

Figure 14. Global meridional overturning stream function ψ in Sv. ψ was calculated in density space and remapped to depth levels for ICON (a-d), FESOM (e-h), and MITgcm (i-l).

forcing C is the strongest, and A and B are similar. This difference represents the current uncertainty of the energy flux into the wave field.

The three ocean models and their configurations in this work are meant as examples of typical state-of-the-art non-eddy-resolving ocean-only global configurations. The surface forcing of the models is identical, while many other aspects of the models differ. We reiterate that no attempt has been made to tune the performance of the new vertical mixing scheme. The effect of the three different bottom forcing functions in the three ocean models is assessed by comparison to a reference simulation, in which the effect of breaking internal gravity waves is implemented by a threshold for minimal turbulent energy. Since the effects of a new parameterization are often model-dependent, the response in the three different models allows us to assess the model-independent effects of the IDEMIX closure. We find the following effects common to all models:

- All model simulations with IDEMIX generate larger interior mixing work κN^2 in the global integral, with more pronounced vertical and, in particular, horizontal structure as a consequence of the inhomogeneous forcing functions, compared to the respective reference simulation (Figs. 2, 3, and 13). The globally underestimated mixing work in the reference simulations could be mitigated by adjusting the threshold of minimal turbulent energy in the scheme of small-scale turbulent mixing. However, the spatial structure can only be reproduced with a mixing scheme that explicitly represents the spatially inhomogeneous internal tide generation, such as IDEMIX. Note that our choice of the minimum TKE threshold value is based on common practice in ocean modeling (e.g., Blanke & Delecluse, 1993).
- IDEMIX improves the horizontal variations of κN^2 along two example transects 170°W and 48°N in the Atlantic Ocean – within the large error bounds – compared to finestructure observations (Figs. 3 and 4). The mixing work obtained with forcing A and B best matches the observations. Simulations with forcing C seem to overestimate κN^2 in the South Pacific and the Southern Ocean and to underestimate it in the subtropical Pacific (Fig. 13). All but the MITgcm simulations tend to overestimate κN^2 in the subpolar North Pacific. The differences of κN^2 between the different forcing functions, however, are smaller than the large error bounds of the observations.

- In all simulations with IDEMIX, the thermocline tends to be deeper compared to the respective reference simulations, although there are also regions with shallower thermocline depths (Fig. 6). This is related to cooling of the upper thermocline and warming of the lower thermocline, but local thermocline depth changes are not necessarily related to locally increased mixing rates but rather resemble patterns of the local stratification. Whether these changes reduce the model-data misfit (i.e., the difference to the initial conditions) depends on the individual model since they may or may not compensate other model biases.
- In the Indo-Pacific, the wind-driven shallow overturning cell within the thermocline increases with IDEMIX (Fig. 12). Due to the deeper thermocline, larger areas of the subducting density layers may be exposed to the atmosphere leading to stronger ventilation and stronger overturning.
- Mixed layer depths in the subpolar North Atlantic are deeper in all IDEMIX simulations. These may be caused by more efficient preconditioning of deep convection (supplementary Fig. 2).
- The increased mixed layer depth in the subpolar North Atlantic is related to an increase in the upper cell of the Atlantic overturning circulation common to all models and improves the agreement with observed transports in the subtropics (Figs. 10 and 12).
- The increase in the upper cell of the Atlantic overturning circulation is associated with an increase in northward heat transport in the Atlantic (Fig. 11), although all models still underestimate northward heat transports.
- Comparing simulations with different bottom forcings shows no substantial differences between forcing A and B, but forcing C, which is strongest in magnitude, leads to a substantial increase of the mixed layer depth in regions of deep convection (most prominent in the Labrador Sea and the Weddel Sea).

There are also responses not common to all models:

- In the Southern Ocean, the energy input in forcing C leads to an unrealistically large region of deep convection in the Weddell Sea in FESOM-C. With the other two forcings, this is not the case (supplementary Fig. 3) and with the other two models a similar effect might be seen but does not have the extreme consequences that it has for FESOM. This artifact points towards too large and unrealistic energy input by forcing C (see Section 6 and Fig. 13b).
- There is no coherent effect of IDEMIX on the lower cell in the Atlantic and the Indo-Pacific, even though the changes are substantial (up to a factor of two) in some of the simulations (Figs. 10 and 12). Note that all models and all simulations start with too low transports of the lower Indo-Pacific cell in the reference solutions. With more mixing work generated by IDEMIX, we expect the lower Indo-Pacific cell to become stronger, but the cell's strength even reduces for ICON, and for FESOM and MITgcm, this cell strengthens only for the strong forcing C but hardly changes for forcings A and B.
- Since all models are subject to different temperature and salinity biases in the references simulations, IDEMIX may or may not reduce those biases. While the temperature bias was largely reduced in ICON-A for example, the corresponding temperature bias was enhanced for FESOM-A and MITgcm-A compared to the reference simulations.

The reason for the circulation bias in the bottom cell of the Indo-Pacific Ocean, and the reason for the incoherent model response in the bottom cell in the Indo-Pacific and Atlantic Ocean are unclear. At the same time, the upper cell in the North Atlantic shows a coherent model response of an increase with stronger mixing work. The increase in the upper cell in the North Atlantic is related to deeper convection in the subpolar North Atlantic, which we, in turn, explain by changes in preconditioning for convection caused by the change in vertical mixing. We cannot answer how changes in convection are related to changes in the strength of the upper cell in the North Atlantic, since there is currently no consistent dynamical framework of the dynamics of the ocean's overturning in closed basins (e.g. Straub, 1996; Greatbatch & Lu, 2003; Brüggemann et al., 2011).

Numerical mixing, typically strong for coarse models, may hide some of the effects of the additional vertical mixing by IDEMIX on the large-scale transports in the bottom overturning cells in the major ocean basins. Other non-local effects may be responsible for the model biases in the bottom cells, such as deep water formation biases around the Antarctic, errors in bottom topography, or errors in the isopycnal structure of the Antarctic Circumpolar Current. Unfortunately, numerical mixing is difficult to assess and requires specific diagnostic methods (e.g. Klingbeil et al., 2014; Banerjee et al., 2023); without them, we have to postpone any further discussion. Nevertheless, our results suggest to revisit water mass transformations and diapycnal velocities associated with numerical mixing.

We find that circulation and bias patterns differ between models despite the similarity of the configurations. Such differences result from the different numerical grids, the different advection schemes, different choices for thickness diffusivity, differences in vertical resolution, and slight differences in interpolated topography, which can have severe consequences on, for example, transports through narrow passages. Despite all these differences, we identified remarkably similar responses of each model once the mixing is changed.

Applying a more realistic vertical mixing parameterization has a notable effect on the ocean circulation with reduced model biases. Owing to the large computational and organizational efforts involved, parameterizations and algorithms are typically only tested in a single ocean model. In this study, we demonstrated in an inter-comparison of ICON, FESOM, and MITgcm the model-independent, positive effect of the internal wave mixing closure IDEMIX. This more realistic mixing parameterization helps to identify model biases since now the energy available for vertical mixing is constrained in a physically consistent way.

Appendix A Vertical mixing closure

In this study, we use a well established 2nd order turbulent kinetic energy (TKE) closure (Gaspar et al., 1990), to parameterize the mixing in the surface mixed layer, but also the mixing in the interior of the ocean in the reference experiments. The closure is based on a parameterized budget for turbulent kinetic energy E_{tke}, assuming laterally homogeneous conditions, given by

$$\partial_t E_{tke} = \partial_z \left(c_{tke} \kappa_m \partial_z E_{tke} \right) + \kappa_m \left(\partial_z \boldsymbol{u} \right)^2 + \epsilon_{iw} - k N^2 - c_\epsilon E_{tke}^{3/2} L^{-1} \tag{A1}$$

with the parameter $c_\epsilon = 0.7$ and $c_{tke} = 30.0$. The dissipation of internal wave energy ϵ_{iw} that is provided by IDEMIX (ϵ_{iw} from Eq. B1 enters Eq. A1 as a source). In the reference experiments without IDEMIX, ϵ_{iw} is derived from the energy input which is necessary to keep the E_{tke} at the prescribed minimum value. A simple parameterization for surface wave breaking is prescribed as Neuman boundary condition for the vertical diffusion term (first term of the r.h.s. in Eq. A1) where the surface flux is set to $c_w \tau^{3/2}$ with $c_w = 3.75$.

Central to the closure is the mixing length assumption for the vertical viscosity $\kappa_m = c_k E_{tke}^{1/2} L$, with $c_k = 0.1$. The choice of the mixing length scale L follows Blanke and Delecluse (1993, their Eqs. 2.27–2.30). The vertical diffusivity to be used in the tracer equations is $\kappa = \kappa_m / Pr$ with the Prandtl number Pr given by

$$\mathrm{Pr} = \max\left(1, \min(10, 6.6\mathrm{Ri})\right), \quad \mathrm{Ri} = N^2 \max\left(\left(\partial_z \boldsymbol{u}\right)^2, \epsilon_{iw}/\kappa_m \right)^{-1}. \tag{A2}$$

This formulation for Pr and the Richardson number Ri yields an interior mixing efficiency of 0.2. In the reference experiments $E_{tke} \longleftarrow \max(E_{tke}, 10^{-6}\,\mathrm{m}^2/\mathrm{s}^2)$ at each time step in addition to the production of E_{tke} by the shear of the mean flow.

Appendix B IDEMIX closure

IDEMIX (Internal Wave Dissipation, Energy and Mixing) is an internal wave model based on the radiative transfer equation, the spectral energy balance equation of internal gravity waves (Olbers & Eden, 2013). Several simplifications, most notably the integration in wavenumber space, reduce the complexity of the radiative transfer equation and lead to partial differential equations for wave energy compartments that are simple enough to be solved online in global ocean general circulation models. Several different versions of IDEMIX have been proposed, including a low-mode tidal and near-inertial wave compartment with explicitly resolved horizontal propagation (Eden & Olbers, 2014), a version including the effect of wave drag on the mean flow (Olbers & Eden, 2017; Eden & Olbers, 2017), and a version including a compartment for lee waves (Eden et al., 2021). In this study, however, we use the simplest IDEMIX approach (Olbers & Eden, 2013), in which all types of internal gravity waves are considered to be part of a horizontally homogeneous continuum. It is given by

$$\partial_t E_{iw} = \partial_z \left(c_0 \tau_v \partial_z c_0 E_{iw} \right) + \nabla_h \cdot \tau_h v_0 \nabla_h v_0 E_{iw} - \epsilon_{iw}. \tag{B1}$$

E_{iw} is the internal wave energy density (the sum of upward and downward propagating energies)c_0 and v_0 are bulk group velocities in vertical and horizontal direction, respectively, calculated assuming a certain spectral shape of the wave field, that is, the Garrett-Munk (GM) model spectrum (Cairns & Williams, 1976; Munk, 1981). $\epsilon_{iw} = \mu_0 f_e \frac{m_*^2}{N^2} E_{iw}^2$ represents the dissipation of wave energy by wave breaking following (Henyey et al., 1986) with $f_e = |f| \mathrm{acosh}(N/|f|)$, and is also used in the finestructure parameterization (Kunze, 2017). Note that this form for ϵ_{iw} was validated recently by Eden et al. (2019) by numerical evaluation of the scattering integral for wave-wave interactions.

The following parameters are contained in our IDEMIX closure:

- τ_v is a time scale on which wave-wave interactions lead to a symmetrization of the energy compartments of up- and downward propagating waves.
- τ_h is a corresponding time scale for eliminating lateral anisotropy.
- μ_0 is related to the dissipation of internal wave energy by wave-wave interactions.
- j_* is the equivalent mode number scale, related to the roll-off wavenumber m_* in the GM model spectrum by $m_* = N/c_*$ with $c_* = \int N/(j_* \pi) \mathrm{d}z$.

The parameter settings that lead to the best agreement with maps of wave energy and E_{tke} dissipation rates estimated from Argo float profiles are $\tau_v = 2\,\mathrm{d}$, $\tau_h = 15\,\mathrm{d}$, $\mu_0 = 1/3$ and $j_* = 5$ (Pollmann et al., 2017). Sensitivity tests indicate that variations of τ_v and τ_h have very little impact on the average wave energy levels and TKE dissipation rates, whereas variations of j_* have the largest (Pollmann et al., 2017). Through its impact on the representative vertical group velocity, higher values of j_* will reduce the upper-ocean internal wave energy levels.

In IDEMIX, internal wave energy is generated at the vertical boundaries and implemented as boundary conditions for the flux divergence term, the first term on the right-hand side of Eq. B1: at the surface, wind stress fluctuations create near-inertial oscillations of the mixed layer that can radiate internal waves of near-inertial frequency into the ocean interior, and at the bottom, the interaction of barotropic tidal currents with rough seafloor topography leads to the formation of internal tides. For the former, we update the maps used by Olbers and Eden (2013) and take instead the fraction of wind power input into near-inertial motions that leaves the mixed layer following Rimac et al. (2013) and shown in Fig. 1a. For the latter, we use three different maps, which are shown in Fig. 1b–d.

Appendix C Tidal forcing

Tidal forcing in IDEMIX is a two-dimensional map of the barotropic-to-baroclinic energy conversion applied at the bottom. This energy conversion can be estimated in several ways: from linear theory (Bell, 1975a, 1975b), from a simple scaling based on linear theory to describe the dissipation in barotropic tide models (Arbic et al., 2018), or from three-dimensional numerical simulations forced with the lunisolar tidal potential (Niwa & Hibiya, 2011; Müller et al., 2010; Buijsman et al., 2020).

Forcing C is a simple relation for the barotropic-to-baroclinic tidal energy conversion based on linear theory:

$$E_f = \frac{1}{2}\rho_0 k_{topo} h^2 N |\mathbf{u}|^2, \tag{C1}$$

where h^2 is the variance of the bottom roughness, ρ_0 the density, N the buoyancy frequency, $\mathbf{u} = (u, v)$ is the horizontal velocity vector and k_{topo} the topographic wavenumber treated as a free, spatially constant parameter (Jayne & St. Laurent, 2001). It was suggested by Jayne and St. Laurent (2001) to add an associated drag term $-1/2k_{topo}h^2N\mathbf{u}$ as a sink to the barotropic shallow water momentum budget to account for the energy loss by internal tide generation, which led to a much better agreement with barotropic tide dissipation estimates obtained from satellite altimetry. The scaling Eq. C1 is often used in parameterizations of near-field tidal mixing in global numerical simulations (St. Laurent et al., 2002; Simmons et al., 2004; Griffies et al., 2015) and, evaluated globally for the Community Earth System Model (CESM) (Hurrell et al., 2013), also as tidal forcing in IDEMIX (Olbers & Eden, 2013). The latter is what we use as forcing C. As eq. C1 was obtained by neglecting any frequency dependence (Jayne & St. Laurent, 2001), forcing C represents all tidal constituents.

Forcing B is derived from linear theory, which builds on the work of Bell (1975a, 1975b). While Bell assumes an infinitely deep ocean, Llewellyn Smith and Young (2002) as well as Khatiwala (2003) considered a finite depth ocean and derived the conversion into different vertical normal modes. These expressions or variants thereof have been evaluated globally a number of times: Nycander (2005), for example, performed global calculations for the 8 major constituents using Bell's theory, to which he applied a correction factor to mimic the behavior in a finitely deep ocean. Falahat et al. (2014) calculated the conversion globally for the first 10 M_2-tide modes using the approach of Llewellyn Smith and Young (2002). Other evaluations include the computation of the first 50 modes of the global M_2-tide generation by Vic et al. (2019) and the directional mode-1 M_2 generation of Pollmann and Nycander (2023). All linear theory approaches rely on several assumptions, i.a. that the topography be subcritical (that is, less steep than the tidal beams), the topographic obstacles be much smaller than the water depth, and the tidal excursion be small. To date, there is no analytically sound derivation of how to correct the relevant equations in cases when these assumptions are violated; instead, the calculations are performed everywhere and empirical corrections are added later (e.g. Falahat et al., 2014) or problematic regions are masked in the compuations (Pollmann & Nycander, 2023). The advantage of the linear theory approach is that topography input of very high resolution can be used at reasonable computational costs. Here, we use the non-modal linear theory estimates of Nycander (2005) as calculated by Falahat et al. (2014) as forcing B, which represent the eight major tidal constituents M_2, S_2, N_2, K_2, K_1, O_1, P_1, Q_1.

Forcing A is derived from a three-dimensional numerical model forced with the lunisolar tidal potential. The advantage of this approach (Niwa & Hibiya, 2011; Müller et al., 2010; Buijsman et al., 2020) is that all the assumptions inherent in linear theory are irrelevant, but on the downside, not all modes are resolved and different assumptions to handle the dissipation of the internal tide energy are necessary. For forcing A, we consider the M_2-tide generation in the STORMTIDE2 simulation (Li & von Storch, 2020). STORMTIDE2 was performed using the primitive-equation Max-Planck-Institute Ocean Model (MPI-OM) (Marsland et al., 2003; Jungclaus et al., 2006) with a horizontal resolution of 0.1° and 40 vertical levels to resolve the lowest modes of the M_2-tide. Tides are excited by applying the full luni-solar tidal potential, parameterizing self-attraction and loading effects following Thomas et al. (2001). After a 33-year long spin-up with a climatological forcing of daily resolution (Röske, 2006), the model is forced by the 6-hourly NCEP/NCAD reanalysis-1 (Kalnay et al., 1996) and integrated for the years 1981-2012. The barotropic-to-baroclinic energy conversion of the M_2-tide was evaluated for the final year of this period. Li et al. (2015) show that the STORMTIDE simulation fully resolves the propagation of the first two M_2 tide modes. It is likely that more modes are resolved when it comes to their generation, but it is unclear how many exactly. Because the lowest modes carry most of the energy, we will in our comparison of the different tidal forcings for IDEMIX not make any correction for the unresolved higher M_2-modes and only add the seven most important other constituents of the computation by Nycander (2005) to obtain a total forcing agreeing with forcings C and B.

Open Research Section

The model code of ICON-O is available to individuals under licenses (`https://mpimet.mpg.de/en/science/modeling-with-icon/code-availability`). By downloading the ICON source code, the user accepts the licence agreement. The model code for FESOM was obtained from S. Scholz P. Dmitry et al. (2023). The model code for MITgcm can be found under `https://github.com/MITgcm/MITgcm`, specific modifications, configuration, and plotting scripts can be found under `https://github.com/mjlosch/MITgcm/tree/idemix_test_runs`.

The source code of the specific ICON-O version used in this study, the configuration files for the ICON-O simulations, and the post-processing scripts for ICON-O, FESOM, and MITgcm, the observational data and scripts for visualization, and the surface forcing data for IDEMIX can be found under `https://hdl.handle.net/21.11116/0000-000C-DE5C-4`. The ICON-O plots were made by making use of the ICON post-processing toolbox pyicon (`https://gitlab.dkrz.de/m300602/pyicon`) and the FESOM plots were made by making use of tripyview (`https://github.com/FESOM/tripyview`).

The CVMix implementation of IDEMIX and the TKE scheme which are used by ICON-O and FESOM can be found within the corresponding model source codes and under `https://github.com/nbruegge/CVMix-src`. MITgcm used an equivalent implementation of IDEMIX and the TKE scheme that can be found within the MITgcm source code (see link above).

The tidal forcing of Nycander (2005) and Falahat et al. (2014) was obtained from Falahat et al. (2018), using the corrected form of the modal calculations of Falahat et al. (2014) provided by de Lavergne et al. (2019). The tidal forcing based on the scaling by Jayne (2009) is the same as used in CESM simulations, which we obtained from their subversion server `https://svn-ccsm-inputdata.cgd.ucar.edu/trunk/inputdata/ocn/pop/gx1v6/forcing/`.

The full-depth observational references were obtained from `https://ftp.nwra.com/outgoing/kunze/iwturb/` (Kunze, 2017) and (Mertens et al., 2019; Mertens et al., 2020). The global map of observed mixing work, available from `https://hdl.handle.net/21.11116/0000-000C-DE5C-4`, was derived as an update of Pollmann et al. (2023) for global estimates of energy levels and TKE dissipation Pollmann et al. (2017) using hydrographic profiles collected by Argo floats (Argo, 2000). These data were collected and made freely available by the International Argo Program and the national programs that contribute to it (https://argo.ucsd.edu, https://www.ocean-ops.org). The Argo Program is part of the Global Ocean Observing System. The global topography dataset of Becker et al. (2009) can be downloaded from `https://topex.ucsd.edu/marine_topo/`.

Acknowledgments

We would like to thank three anonymous reviewers whose comments substantially improved our manuscript. This paper is a contribution to the Collaborative Research Centre TRR 181 "Energy Transfers in Atmosphere and Ocean" funded by the Deutsche Forschungsgemeinschaft (DFG, German Research Foundation) - Projektnummer 274762653. This work used resources of the Deutsches Klimarechenzentrum (DKRZ) granted by its Scientific Steering Committee (WLA) under project ID bm1239.

References

Adcroft, A., & Campin, J.-M. (2004). Rescaled height coordinates for accurate representation of free-surface flows in ocean circulation models. *Ocean Modelling*, *7*(3), 269–284. doi: 10.1016/j.ocemod.2003.09.003

Ansong, J. K., Arbic, B. K., Simmons, H. L., Alford, M. H., Buijsman, M. C., Timko, P. G., ... Wallcraft, A. J. (2018). Geographical distribution of diurnal and semidiurnal parametric subharmonic instability in a global ocean circulation model. *Journal of Physical Oceanography*, *48*(6), 1409–1431.

Arbic, B. K., Alford, M. H., Ansong, J. K., Buijsman, M. C., Ciotti, R. B., Farrar, J. T., ... others (2018). A primer on global internal tide and internal gravity wave continuum modeling in HYCOM and MITgcm. *New frontiers in operational oceanography*.

Argo. (2000). *Argo float data and metadata from Global Data Assembly Centre (Argo GDAC). SEANOE.* [Dataset]. doi: https://doi.org/10.17882/42182

Banerjee, T., Danilov, S., & Klingbeil, K. (2023). *Discrete variance decay analysis of spurious mixing.*

Baumann, T. M., Fer, I., Schulz, K., & Mohrholz, V. (2023). Validating finescale parameterizations for the eastern Arctic Ocean internal wave field. *Journal of Geophysical Research: Oceans*, *128*(11), e2022JC018668.

Becker, J., Sandwell, D., Smith, W., Braud, J., Binder, B., Depner, J., ... others (2009). Global bathymetry and elevation data at 30 arc seconds resolution: Srtm30_plus [Dataset]. *Marine Geodesy*, *32*(4), 355–371.

Bell, T. (1975a). Lee waves in stratified flows with simple harmonic time dependence. *J. Fluid Mech.*, *67*(4), 705–722.

Bell, T. (1975b). Topographically generated internal waves in the open ocean. *J. Geophys. Res.*, *80*(3), 320–327.

Blanke, B., & Delecluse, P. (1993). Variability of the tropical Atlantic Ocean simulated by a general circulation model with two different mixed-layer physics. *Journal of Physical Oceanography*, *23*(7), 1363–1388.

Brüggemann, N., Eden, C., & Olbers, D. (2011). A dynamically consistent closure for zonally averaged ocean models. *J. Phys. Oceanogr.*, *41*(11), 2242–2258.

Brüggemann, N., & Katsman, C. A. (2019, September). Dynamics of downwelling in an eddying marginal sea: Contrasting the eulerian and the isopycnal perspective. *J. Phys. Oceanogr.*, *49*(11), 3017–3035. doi: 10.1175/jpo-d-19-0090.1

Buijsman, M. C., Stephenson, G. R., Ansong, J. K., Arbic, B. K., Green, J. M., Richman, J. G., ... Zhao, Z. (2020). On the interplay between horizontal resolution and wave drag and their effect on tidal baroclinic mode waves in realistic global ocean simulations. *Ocean Modelling*, *152*, 101656.

Cairns, J. L., & Williams, G. O. (1976). Internal wave observations from a midwater float. *J. Geophys. Res.*, *81*(12), 1943–1950.

Crawford, G., & Large, W. (1996). A numerical investigation of resonant inertial response of the ocean to wind forcing. *Journal of Physical Oceanography*, *26*(6), 873–891.

Danilov, S., Sidorenko, D., Wang, Q., & Jung, T. (2017). The finite-volume sea ice–ocean model (FESOM2). *Geoscientific Model Development*, *10*(2), 765–789.

de Lavergne, C., Groeskamp, S., Zika, J., & Johnson, H. L. (2022). Chapter 3 - the role of mixing in the large-scale ocean circulation. In M. Meredith & A. Naveira Garabato (Eds.), *Ocean mixing* (p. 35-63). Elsevier. Retrieved from `https://www.sciencedirect.com/science/article/pii/B9780128215128000104` doi: https://doi.org/10.1016/B978-0-12-821512-8.00010-4

de Lavergne, C., Falahat, S., Madec, G., Roquet, F., Nycander, J., & Vic, C. (2019). Toward global maps of internal tide energy sinks. *Ocean Modelling*, *137*, 52–75.

de Lavergne, C., Vic, C., Madec, G., Roquet, F., Waterhouse, A. F., Whalen, C., . . . Hibiya, T. (2020). A parameterization of local and remote tidal mixing. *Journal of Advances in Modeling Earth Systems*, *12*(5), e2020MS002065.

Eden, C., & Jung, T. (2001). North Atlantic interdecadal variability: oceanic response to the North Atlantic Oscillation (1865–1997). *Journal of Climate*, *14*(5), 676–691.

Eden, C., & Olbers, D. (2014). An energy compartment model for propagation, nonlinear interaction, and dissipation of internal gravity waves. *Journal of Physical Oceanography*, *44*(8), 2093–2106.

Eden, C., & Olbers, D. (2017). A closure for internal wave–mean flow interaction. Part II: Wave drag. *Journal of Physical Oceanography*, *47*(6), 1403–1412.

Eden, C., Olbers, D., & Eriksen, T. (2021). A closure for lee wave drag on the large-scale ocean circulation. *Journal of Physical Oceanography*, *51*(12), 3573–3588.

Eden, C., Pollmann, F., & Olbers, D. (2019). Numerical evaluation of energy transfers in internal gravity wave spectra of the ocean. *Journal of Physical Oceanography*, *49*(3), 737–749.

Egbert, G. D., & Erofeeva, S. Y. (2002). Efficient inverse modeling of barotropic ocean tides. *J. Atmos. Oceanic Technol.*, *19*(2), 183–204.

Falahat, S., Nycander, J., de Lavergne, C., Roquet, F., Madec, G., & Vic, C. (2018). *Global estimates of internal tide generation rates at 1/30° resolution.* Retrieved from `https://doi.org/10.17882/58153` doi: 10.17882/58153

Falahat, S., Nycander, J., Roquet, F., & Zarroug, M. (2014). Global calculation of tidal energy conversion into vertical normal modes. *J. Phys. Oceanogr.*, *44*(12), 3225–3244. doi: https://doi.org/10.1175/JPO-D-14-0002.1

Ferreira, D., Marshall, J., & Heimbach, P. (2005). Estimating eddy stresses by fitting dynamics to observations using a residual-mean ocean circulation model and its adjoint. *J. Phys. Oceanogr.*, *35*, 1891-1910.

Fleury, M., & Lueck, R. (1994). Direct heat flux estimates using a towed vehicle. *Journal of physical oceanography*, *24*(4), 801–818.

Forget, G., Campin, J.-M., Heimbach, P., Hill, C. N., Ponte, R. M., & Wunsch, C. (2015). ECCO version 4: an integrated framework for non-linear inverse modeling and global ocean state estimation. *Geoscientific Model Development*, *8*(10), 3071–3104. doi: 10.5194/gmd-8-3071-2015

Ganachaud, A. (2003). Large-scale mass transports, water mass formation, and diffusivities estimated from world ocean circulation experiment (woce) hydrographic data. *J. Geophys. Res.*, *108*(C7). doi: 10.1029/2002JC001565

Garrett, C., & Munk, W. (1972). Space-Time scales of internal waves. *Geophysical Fluid Dynamics*, *3*(3), 225-264. doi: 10.1080/03091927208236082

Gaspar, P., Grégoris, Y., & Lefevre, J.-M. (1990). A simple eddy kinetic energy model for simulations of the oceanic vertical mixing: Tests at station Papa and long-term upper ocean study site. *J. Geophys. Res. Oceans*, *95*(C9), 16179–16193. doi: 10.1029/JC095iC09p16179

Gent, P. R., Willebrand, J., McDougall, T. J., & McWilliams, J. C. (1995). Parameterizing eddy-induced tracer transports in ocean circulation models. *Journal of Physical Oceanography*, *25*(4), 463–474.

Georgiou, S., Ypma, S. L., Brüggemann, N., Sayol, J.-M., van der Boog, C. G., Spence, P., … Katsman, C. A. (2021, January). Direct and indirect pathways of convected water masses and their impacts on the overturning dynamics of the labrador sea. *J. Geophys. Res. Oceans*, *126*(1), e2020JC016654. doi: 10.1029/2020JC016654

Greatbatch, R., & Lu, J. (2003). Reconciling the Stommel Box Model with the Stommel–Arons Model: A Possible Role for Southern Hemisphere Wind Forcing? *J. Phys. Oceanogr.*, *33*, 1618–1632.

Gregg, M. C. (1989). Scaling turbulent dissipation in the thermocline. *Journal of Geophysical Research: Oceans*, *94*(C7), 9686–9698.

Griffies, S. M., Levy, M., Adcroft, A. J., Danabasoglu, G., Hallberg, R. W., Jacobsen, D., … Ringler, T. (2015). *Theory and numerics of the community ocean vertical mixing (cvmix) project [software]* ( ). : NOA/GFDL, NCAR, LANL.

Gutjahr, O., Brüggemann, N., Haak, H., Jungclaus, J. H., Putrasahan, D. A., Lohmann, K., & von Storch, J.-S. (2021). Comparison of ocean vertical mixing schemes in the Max Plank Institute Earth System Model (MPI-ESM1.2). *Geoscientific Model Development Discussions*, *2020*, 1–47. Retrieved from https://gmd.copernicus.org/preprints/gmd-2020-202/ doi: 10.5194/gmd-2020-202

Henyey, F., Wright, J., & Flatté, S. (1986). Energy and action flow through the internal wave field: An eikonal approach. *J. Geophys. Res.*, *91*(C7), 8487–8495.

Hohenegger, C., Korn, P., Linardakis, L., Redler, R., Schnur, R., Adamidis, P., … Stevens, B. (2023). Icon-sapphire: simulating the components of the earth system and their interactions at kilometer and subkilometer scales. *Geoscientific Model Development*, *16*(2), 779–811. doi: 10.5194/gmd-16-779-2023

Hurrell, J. W., Holland, M. M., Gent, P. R., Ghan, S., Kay, J. E., Kushner, P. J., … others (2013). The community earth system model: a framework for collaborative research. *Bull. Amer. Meteor. Soc.*, *94*(9), 1339–1360.

Jayne, S. R. (2009). The impact of abyssal mixing parameterizations in an ocean general circulation model. *J. Phys. Oceanogr.*, *39*(7), 1756–1775. doi: https://doi.org/10.1175/2009JPO4085.1

Jayne, S. R., & St. Laurent, L. C. (2001). Parameterizing tidal dissipation over rough topography. *Geophys. Res. Lett.*, *28*(5), 811–814. doi: https://doi.org/10.1029/2000GL012044

Jungclaus, J. H., Keenlyside, N., Botzet, M., Haak, H., Luo, J.-J., Latif, M., … Roeckner, E. (2006). Ocean circulation and tropical variability in the coupled model ECHAM5/MPI-OM. *Journal of climate*, *19*(16), 3952–3972.

Jungclaus, J. H., Lorenz, S. J., Schmidt, H., Brovkin, V., Brüggemann, N., Chegini, F., … others (2022). The ICON earth system model version 1.0. *Journal of Advances in Modeling Earth Systems*, *14*(4), e2021MS002813.

Kalnay, E., Kanamitsu, M., Kistler, R., Collins, W., Deaven, D., Gandin, L., … others (1996). The NCEP/NCAR 40-year reanalysis project. *Bull. Amer. Meteor. Soc.*, *77*(3), 437–472.

Kelly, S., & Nash, J. (2010). Internal-tide generation and destruction by shoaling internal tides. *Geophysical Research Letters*, *37*(23).

Khatiwala, S. (2003). Generation of internal tides in an ocean of finite depth: analytical and numerical calculations. *Deep-Sea Res.*, *50*(1), 3–21.

Klingbeil, K., Mohammadi-Aragh, M., Gräwe, U., & Burchard, H. (2014). Quantification of spurious dissipation and mixing–discrete variance decay in a finite-volume framework. *Ocean Modelling*, *81*, 49–64.

Korn, P. (2018). A structure-preserving discretization of ocean parametrizations on unstructured grids. *Ocean Modelling*, *132*, 73–90.

Korn, P., Brüggemann, N., Jungclaus, J. H., Lorenz, S., Gutjahr, O., Haak, H., . . . others (2022). ICON-O: The ocean component of the ICON earth system model—global simulation characteristics and local telescoping capability. *Journal of Advances in Modeling Earth Systems*, *14*(10), e2021MS002952.

Kunze, E. (2017). Internal-wave-driven mixing: Global geography and budgets. *J. Phys. Oceanogr.*, *47*(6), 1325–1345.

Kunze, E., Firing, E., Hummon, J. M., Chereskin, T. K., & Thurnherr, A. M. (2006). Global abyssal mixing inferred from lowered adcp shear and ctd strain profiles. *Journal of Physical Oceanography*, *36*(8), 1553–1576.

Large, W. G., McWilliams, J. C., & Doney, S. C. (1994). Oceanic vertical mixing: A review and a model with a nonlocal boundary layer parameterization. *Rev. Geophys.*, *32*(4), 363–403.

Large, W. G., & Yeager, S. G. (2009). The global climatology of an interannually varying air–sea flux data set [Dataset]. *Clim. Dyn.*, *33*, 341–364. doi: https://doi.org/10.1007/s00382-008-0441-3

Li, Z., Storch, J.-S. v., & Müller, M. (2015). The M2 internal tide simulated by a 1/10° OGCM. *J. Phys. Oceanogr.*, *45*(12), 3119–3135.

Li, Z., & von Storch, J.-S. (2020). M2 Internal-Tide Generation in STORMTIDE2. *J. Geophys. Res. Oceans*, *125*(8), e2019JC015453. doi: https://doi.org/10.1029/2019JC015453

Llewellyn Smith, S. G., & Young, W. (2002). Conversion of the barotropic tide. *J. Phys. Oceanogr.*, *32*(5), 1554–1566.

Locarnini, M., Mishonov, A., Baranova, O., Boyer, T., Zweng, M., Garcia, H., . . . others (2018). *World Ocean Atlas 2018, Volume 1: Temperature* [Dataset].

Lozier, M. S., Li, F., Bacon, S., Bahr, F., Bower, A. S., Cunningham, S. A., . . . Zhao, J. (2019, February). A sea change in our view of overturning in the subpolar North Atlantic. *Science*, *363*(6426), 516–521. Retrieved from `http://science.sciencemag.org/content/363/6426/516.abstract`

Lumpkin, R., & Speer, K. (2007). Global ocean meridional overturning. *J. Phys. Oceanogr.*, *37*(10), 2550–2562.

Marshall, J., Adcroft, A., Hill, C., Perelman, L., & Heisey, C. (1997). A finite-volume, incompressible navier stokes model for studies of the ocean on parallel computers. *J. Geophys. Res.*, *102*(C3), 5753–5766. doi: 10.1029/96JC02775

Marsland, S. J., Haak, H., Jungclaus, J. H., Latif, M., & Röske, F. (2003). The Max-Planck-Institute global ocean/sea ice model with orthogonal curvilinear coordinates. *Ocean Modelling*, *5*(2), 91–127.

McDougall, T. J., & McIntosh, P. C. (2001). The temporal-residual-mean velocity. Part II: Isopycnal interpretation and the tracer and momentum equations. *Journal of Physical Oceanography*, *31*(5), 1222–1246.

Melet, A. V., Hallberg, R., & Marshall, D. P. (2022). The role of ocean mixing in the climate system. In *Ocean mixing* (pp. 5–34). Elsevier.

Mertens, C., Köhler, J., Walter, M., von Storch, J.-S., & Rhein, M. (2019). Observations and Models of Low-Mode Internal Waves in the Ocean. In C. Eden & A. Iske (Eds.), *Energy Transfers in Atmosphere and Ocean* (pp. 127–143). Cham: Springer International Publishing. doi: 10.1007/978-3-030-05704-6_4

Mertens, C., Rhein, M., Roessler, A., Kieke, D., & Nowitzki, H. (2020). *Lowered ADCP data at 47°N in the subpolar North Atlantic.* PANGAEA. Retrieved from `https://doi.org/10.1594/PANGAEA.922859` doi: 10.1594/PANGAEA.922859

MITgcm Group. (2022). *MITgcm User Manual* (Online documentation). Cambridge, MA 02139, USA: MIT/EAPS. (`https://mitgcm.readthedocs.io/en/latest`) doi: 10.5281/zenodo.1409237

Müller, M., Haak, H., Jungclaus, J., Sündermann, J., & Thomas, M. (2010). The effect of ocean tides on a climate model simulation. *Ocean Modelling*, *35*(4),

304–313.
Müller, P., Holloway, G., Henyey, F., & Pomphrey, N. (1986, August). Nonlinear interactions among internal gravity waves. *Rev. Geophys.*, *24*(3), 493–536. doi: 10.1029/RG024i003p00493
Munk, W. (1981). Internal waves and small-scale processes. In B. A. Warren & C. Wunsch (Eds.), *Evolution of physical oceanography* (pp. 264–291). MIT Press, Cambridge, MA.
Musgrave, R., Pollmann, F., Kelly, S., & Nikurashin, M. (2022). The lifecycle of topographically-generated internal waves. In *Ocean mixing* (pp. 117–144). Elsevier.
Niwa, Y., & Hibiya, T. (2011). Estimation of baroclinic tide energy available for deep ocean mixing based on three-dimensional global numerical simulations. *J. Oceanogr.*, *67*(4), 493–502.
Nycander, J. (2005). Generation of internal waves in the deep ocean by tides. *J. Geophys. Res. Oceans*, *110*(C10). doi: https://doi.org/10.1029/2004JC002487
Olbers, D. (1983). Models of the oceanic internal wave field. *Rev. Geophys.*, *21*(7), 1567–1606. doi: 10.1029/RG021i007p01567
Olbers, D., & Eden, C. (2013). A global model for the diapycnal diffusivity induced by internal gravity waves. *J. Phys. Oceanogr.*, *43*(8), 1759–1779. doi: https://doi.org/10.1175/JPO-D-12-0207.1
Olbers, D., & Eden, C. (2017). A closure for internal wave–mean flow interaction. Part I: Energy conversion. *Journal of Physical Oceanography*, *47*(6), 1389–1401.
Olbers, D., Eden, C., Becker, E., Pollmann, F., & Jungclaus, J. (2019). The IDEMIX model: Parameterization of internal gravity waves for circulation models of ocean and atmosphere. *Energy Transfers in Atmosphere and Ocean*, 87–125.
Olbers, D., Jurgenowski, P., & Eden, C. (2020). A wind-driven model of the ocean surface layer with wave radiation physics. *Ocean Dyn.*, *70*(8), 1067–1088.
Pacanowski, R., & Philander, S. (1981). Parameterization of vertical mixing in numerical models of tropical oceans. *J. Phys. Oceanogr.*, *11*(11), 1443–1451.
Pollmann, F., Eden, C., & Olbers, D. (2017). Evaluating the global internal wave model IDEMIX using finestructure methods. *J. Phys. Oceanogr.*, *47*(9), 2267–2289.
Pollmann, F., Eden, C., & Olbers, D. (2023). *Global finestructure estimates of internal wave energy levels and wave-induced mixing from argo float profiles.* Retrieved from `https://doi.org/10.17882/95327` doi: 10.17882/95327
Pollmann, F., & Nycander, J. (2023). Resolving the horizontal direction of internal tide generation: Global application for the M2 tide's first mode. *Journal of Physical Oceanography*, *53*(5), 1251–1267.
Polzin, K. L. (2009). An abyssal recipe. *Ocean Modelling*, *30*(4), 298–309.
Polzin, K. L., & Lvov, Y. V. (2011). Toward Regional Characterizations of the Oceanic Internal Wavefield. *Rev. Geophys.*, *49*(4), RG4003–.
Polzin, K. L., Naveira Garabato, A. C., Huussen, T. N., Sloyan, B. M., & Waterman, S. (2014). Finescale parameterizations of turbulent dissipation. *J. Geophys. Res. Oceans*, *119*(2), 1383–1419.
Polzin, K. L., Toole, J. M., & Schmitt, R. W. (1995). Finescale parameterizations of turbulent dissipation. *Journal of physical oceanography*, *25*(3), 306–328.
Quinn, B., Eden, C., Olbers, D., Voelker, G., & Achatz, U. (2023). The transient IDEMIX model as a nonorographic gravity wave parameterization in an atmospheric circulation model. *arXiv preprint arXiv:2311.13555*.
Redi, M. H. (1982). Oceanic isopycnal mixing by coordinate rotation. *J. Phys. Oceanogr.*, *12*(10), 1154–1158. doi: 10.1175/1520-0485(1982)012⟨1154:OIMBCR⟩2.0.CO;2

Rimac, A., Von Storch, J.-S., & Eden, C. (2016). The total energy flux leaving the ocean's mixed layer. *Journal of Physical Oceanography*, *46*(6), 1885–1900.

Rimac, A., von Storch, J.-S., Eden, C., & Haak, H. (2013). The influence of high-resolution wind stress field on the power input to near-inertial motions in the ocean. *Geophys. Res. Lett.*, *40*(18), 4882–4886. doi: 10.1002/grl.50929

Röske, F. (2006). A global heat and freshwater forcing dataset for ocean models [Dataset]. *Ocean Modelling*, *11*(3-4), 235–297.

Saha, S., Moorthi, S., Pan, H.-L., Wu, X., Wang, J., Nadiga, S., ... Goldberg, M. (2010). The NCEP Climate Forecast System Reanalysis. *Bulletin of the American Meteorological Society*, *91*(8), 1015 - 1058. doi: https://doi.org/10.1175/2010BAMS3001.1

Schlitzer, R. (2007). Assimilation of radiocarbon and chlorofluorocarbon data to constrain deep and bottom water transports in the World Ocean. *Journal of Physical Oceanography*, *37*(2), 259–276. Retrieved from `https://journals.ametsoc.org/view/journals/phoc/37/2/jpo3011.1.xml` doi: 10.1175/JPO3011.1

Scholz, P., Sidorenko, D., Danilov, S., Wang, Q., Koldunov, N., Sein, D., & Jung, T. (2022). Assessment of the Finite-VolumE Sea ice–Ocean Model (FESOM2.0) – Part 2: Partial bottom cells, embedded sea ice and vertical mixing library CVMix. *Geosci. Model Dev.*, *15*, 335–363. doi: https://doi.org/10.5194/gmd-15-335-2022

Scholz, S., P. Dmitry, Nikolay, K., Hegewald, J., Rakowsky, N., Streffing, J., Rackow, T., ... Cheedela, S. K. (2023, March). *Fesom/fesom2: Fesom2.5* [Software]. Zenodo. Retrieved from `https://doi.org/10.5281/zenodo.7737061` doi: 10.5281/zenodo.7737061

Simmons, H. L., Jayne, S. R., Laurent, L. C. S., & Weaver, A. J. (2004). Tidally driven mixing in a numerical model of the ocean general circulation. *Ocean Modelling*, *6*(3-4), 245–263.

Smeed, D. A., Josey, S. A., Beaulieu, C., Johns, W. E., Moat, B. I., Frajka-Williams, E., ... McCarthy, G. D. (2018). The North Atlantic Ocean is in a state of reduced overturning. *Geophysical Research Letters*, *45*(3), 1527-1533. doi: https://doi.org/10.1002/2017GL076350

Steele, M., Morley, R., & Ermold, W. (2001). PHC: A global ocean hydrography with a high-quality Arctic Ocean. *J. Climate*, *14*, 2,079–2,087.

St. Laurent, L., Simmons, H., & Jayne, S. (2002). Estimating tidally driven mixing in the deep ocean. *Geophys. Res. Lett.*, *29*(23), 21–1.

Straub, D. (1996). An inconsistency between two classical models of the ocean buoyancy driven circulation. *Tellus A*, *48*(3), 477–481.

Talley, L. D., Reid, J. L., & Robbins, P. E. (2003). Data-Based Meridional Overturning Streamfunctions for the Global Ocean. *J. Climate*, *16*(19), 3213–3226. doi: 10.1175/1520-0442(2003)016⟨3213:DMOSFT⟩2.0.CO;2

Thomas, M., Sündermann, J., & Maier-Reimer, E. (2001). Consideration of ocean tides in an OGCM and impacts on subseasonal to decadal polar motion excitation. *Geophys. Res. Lett.*, *28*(12), 2457–2460.

Tsujino, H., Urakawa, S., Nakano, H., Small, R. J., Kim, W. M., Yeager, S. G., ... Yamazaki, D. (2018). JRA-55 based surface dataset for driving ocean–sea-ice models (JRA55-do). *Ocean Modelling*, *130*, 79-139. doi: https://doi.org/10.1016/j.ocemod.2018.07.002

Vic, C., Naveira Garabato, A. C., Green, J. M., Waterhouse, A. F., Zhao, Z., Melet, A., ... Stephenson, G. R. (2019). Deep-ocean mixing driven by small-scale internal tides. *Nature communications*, *10*(1), 2099.

Visbeck, M., Marshall, J., Haine, T., & Spall, M. (1997). Specification of Eddy Transfer Coefficients in Coarse-Resolution Ocean Circulation Models. *J. Phys. Oceanogr.*, *27*(3), 381–402. doi: 10.1175/1520-0485(1997)027⟨0381:SOETCI⟩2.0.CO;2

von Storch, J.-S., & Lüschow, V. (2023). Wind power input to ocean near-inertial waves diagnosed from a 5-km global coupled atmosphere-ocean general circulation model. *J. Geophys. Res. Oceans*, *128*(2), e2022JC019111. doi: 10.1029/2022JC019111

Waterhouse, A. F., MacKinnon, J. A., Nash, J. D., Alford, M. H., Kunze, E., Simmons, H. L., … others (2014). Global patterns of diapycnal mixing from measurements of the turbulent dissipation rate. *Journal of Physical Oceanography*, *44*(7), 1854–1872.

Whalen, C. B., MacKinnon, J. A., Talley, L. D., & Waterhouse, A. F. (2015). Estimating the mean diapycnal mixing using a finescale strain parameterization. *Journal of Physical Oceanography*, *45*(4), 1174–1188.

Wijesekera, H., Padman, L., Dillon, T., Levine, M., Paulson, C., & Pinkel, R. (1993). The application of internal-wave dissipation models to a region of strong mixing. *Journal of physical oceanography*, *23*(2), 269–286.

Wunsch, C., & Ferrari, R. (2004). Vertical mixing, energy and the general circulation of the oceans. *Annual Review of Fluid Mechanics*, *36*, 281–314. doi: 10.1146/annurev.fluid.36.050802.122121

Zhai, X., Greatbatch, R. J., & Sheng, J. (2004). Diagnosing the role of eddies in driving the circulation of the northwest Atlantic Ocean. *Geophysical Research Letters*, *31*(23). doi: https://doi.org/10.1029/2004GL021146

Zweng, M., Seidov, D., Boyer, T., Locarnini, M., Garcia, H., Mishonov, A., … others (2019). *World Ocean Atlas 2018, Volume 2: Salinity* [Dataset].